

# A Rationale for Backprojection in Spotlight Synthetic Aperture Radar Image Formation

Jerald L. Bauck, *Life Senior Member, IEEE*

**Abstract**—This note on backprojection for spotlight synthetic aperture radar image formation is mainly pedagogic in purpose and is intended to be accessible. The presentation from first principles is elementary and detailed, beginning with the wave equation and melding wave notions with signal processing notions using a compact and consistent notation throughout. A reflection model is developed including a general expression for the receiver signal which does not depend on a particular transmitted waveform. Then the signal is specialized to monochromatic waves to show how waves and the Fourier transform fit together. In the end the signal is once again generalized so that the theory works for any signal type. Backprojection is shown to reconstruct the wave field that was lost by sampling it at only one point, the receiving antenna. After specializing some details to the synthetic aperture radar geometry, the Projection Slice Theorem is introduced late, after an understanding of the underlying principles is obtained. Computational aspects are considered and it is seen that backprojection and direct Fourier inversion, also known as the polar format algorithm, are fundamentally the same, differing only in some implementation details, albeit significant ones, thus overturning the notion that backprojection is not a Fourier process. Those who might benefit from this paper include people who have worked in this field and who seek a somewhat different point of view from the usual presentation, people in other fields who are unfamiliar with some of the engineering concepts involved, and signal processing engineers who appreciate a bit of wave theory.

**Index Terms**—backprojection, direct Fourier inversion, image processing, image reconstruction, keystone format, polar format, polar format algorithm, projections, projection-slice theorem, Radon transform, signal processing, spotlight synthetic aperture radar

## I. INTRODUCTION

**S**IMILARITIES between spotlight-mode synthetic aperture radar (SAR) and computerized tomography (CT) were illuminated in 1983 [1]. With the parallels drawn between the two fields, researchers in SAR were able to borrow and adapt image reconstruction ideas from CT and some existing SAR algorithms benefited from the new perspective. Some of the closely related CT algorithms that have been borrowed and used extensively are called *backprojection*, *convolution-backprojection*, *filtered backprojection*, or a related method called *filter of backprojections*.

Fig. 1 shows a typical basic set-up and geometry of a spotlight SAR. The radar transmitter-receiver is mounted on

a movable vehicle, typically an airplane or low earth orbiting satellite, which moves around a scene of interest on the ground. The radar's antenna is pointed at the scene, or dwelled, as the aircraft moves, allowing the scene to be interrogated by a structured, designed, electromagnetic pulse which reflects from the ground patch and is then collected and processed by the receiver; the interrogation is repeated over a range of angles. An alternate and older form of SAR is stripmap mode whereby the antenna is not dwelled and thus illuminates a strip of the ground as the platform moves. While stripmap SARs image a larger area than spotlight SAR, the resolution is worse given similar system parameters. Variants include inverse SAR where the radar is considered to be stationary and the target rotates and bistatic or multistatic spotlight SAR whereby the one or more transmitters are in different locations than the one or more receivers. Other SAR modes include scanSAR, sliding spotlight, and interferometric SAR (InSAR). Some radars are able to switch between multiple modes.

There are a number of classic and modern papers and books on SAR but most of them focus on stripmap mode and mention spotlight mode little if at all, for example [2], [3], [4], [5], [6]. Of those that do significantly mention spotlight mode, most discuss mainly or only the polar format algorithm about which we shall have more to say later [7], [8], [9], [10], [11], [12], [13], and [14]. Works with a significant orientation to backprojection are [1] which apparently inspired [15], plus [16], [17], [18], and [19]. Other references to backprojection will be mentioned as needed; backprojection is covered more robustly in the literature than what is indicated here. Backprojection borrows heavily from CT image reconstruction although SAR requires modifications of CT methods as it is a fundamentally different sensing modality. Nonetheless, a wealth of relevant knowledge resides in these and related texts: [20], [21], [22], [23], [24]. Finally, an extensive index of SAR research is kept at [25].

Common but certainly not universal assumptions include using the slant plane which is the plane described by the path of the radar and the center of the ground patch, a flat earth, straight or circular flight paths, the absence of multipath and multiple-time-around echoes, and plane waves. The latter will be discussed shortly but while the others are important in applications they are not germane to the present discussion.

The purpose of this note is mainly pedagogical as the concepts described are known from other sources and even widely known in the SAR community, and the mathematics required to understand those sources is usually not terribly advanced—Fourier transforms, calculus, some signal processing and communications theory, and a little geometry. However, we shall take a rather leisurely path through the details and

Jerry Bauck is a researcher, consultant, and inventor in Tempe, Arizona, USA. E-mail: ieee@my last name.net.

Accepted for publication on July 13, 2021. © 2021 IEEE. Personal use of this material is permitted. Permission from IEEE must be obtained for all other uses, in any current or future media, including reprinting/republishing this material for advertising or promotional purposes, creating new collective works, for resale or redistribution to servers or lists, or reuse of any copyrighted component of this work in other works.

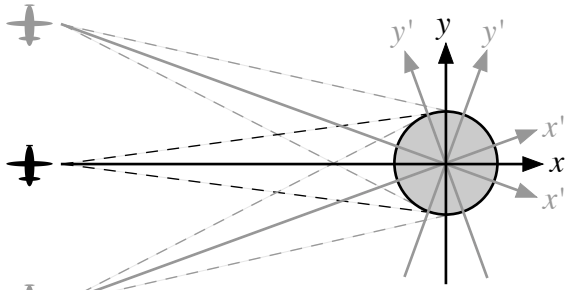


Fig. 1. SAR geometry showing a zero-degree orientation of the radar and two rotated orientations.

ultimately arrive at backprojection by physical reasoning that might provide a different perspective and perhaps a modicum of insight that other writings tend to obscure for the sake of efficiency of exposition.

The note begins with a section which develops a detailed reflection model starting from first principles—the wave equation and a general solution thereto. There is no prejudice as to the particular form of the transmitted signal. This section is very basic and derives results readily stated elsewhere but will serve other purposes in the next section. The next section motivates backprojection by showing that it is the plane wave spectrum reconstruction of a single point scatterer and relates the method to restoring spatial information that is lost by the radar receiver. Throughout, simple cases are developed before more general cases, and at times then the general case will be specialized back to a specific case as regards geometries, signals, and ground patch models.

In this work plane waves are assumed throughout even though the signal emitted by a radar is not planar, even in the far field where it is spherical<sup>1</sup>. While strictly speaking the plane wave assumption is wrong, it is commonly made with a great advantage in analytical simplicity. In practice the plane wave assumption is supported by the fact that the antenna main beam limits the angular extent of the radiated ground patch so that the error caused by actual wavefront curvature over that narrow angle remains small and at least approximately known over the illuminated area, where “small” is related to angular and range resolution, and wavelength. But always, the approximation and its effects are recognized so that results maintain their validity within carefully stated limits of operating parameters. Countless books, for example [14], and papers have been written detailing methods to correct, counteract, focus, and otherwise adjust for the approximation. Alternately, spherical waves, represented by circular intersections with a flat earth, also lend themselves to backprojection methods [27], [28], [29], [30], [31], [32] including elliptical backprojections in the case of bistatic modes. We shall not be concerned with

<sup>1</sup>Some authors describe, without qualification, the far field of a radiating source as being characterized by plane waves and the near field as spherical waves. Both are incorrect; the far field is characterized by spherical waves or by waves approaching sphericity and include a  $1/r$  amplitude dependency. The details are more technical and include noting that higher-order powers of  $1/r$  are increasingly ignorable for large  $r$  [26]. Plane waves, like sine waves, are a convenient fiction.

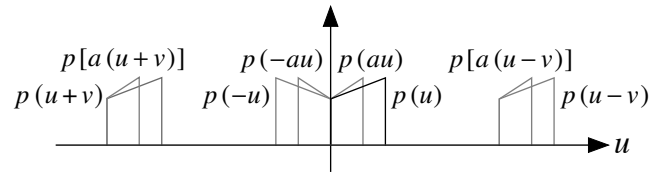


Fig. 2. Examples of shifting and scaling a function. In this example, shift  $v > 0$  and scale  $a > 1$ .

these issues since they are not relevant to the present topic, the plane wave assumption being acceptable for present purposes. Even so, the principles discussed herein can be adapted to the spherical wave assumption but the presentation becomes more complicated.

## II. PROPAGATION AND REFLECTION MODELS

In this section a simple but general solution to the wave equation is developed for the radar application and then a reflection model is developed. Some readers might find the early part of this section too elementary and can skip it but the later result feeds immediately into Section III.

### A. Signal Scaling and Shifting

In the following, signal and wave descriptions will appear with various scale factors and various amounts of shift. These signals can be either time-dependent, space-dependent in one or several dimensions, or both, that is, spatiotemporal signals. It will be useful to review a kind of canonical form for these signal variations. Consider a generic signal  $p(u)$  and versions thereof that are shifted and scaled by various amounts. Fig. 2 shows various shifted and scaled versions of  $p(u)$  based on the canonical form  $p[a(u-v)]$ . In the figure only, it is assumed that scale factor  $a$  and shift amount  $v$  are positive and further that  $a > 1$ . Many times the argument of a function that has simple amounts of scaling and shifting is expressed in various forms but usually the argument can be rewritten in this canonical form that eases interpretation. In the form  $p[a(u-v)]$ ,  $u$  is the independent variable,  $a$  is the scale factor, and  $v$  is the shift amount. With  $a$  and  $v$  both positive, the interpretation is: first, scale  $p$  by  $a$ , then shift right by  $v$ . A negative  $a$  will cause the function to be flipped around the origin as well as scaled, and a negative  $v$  will cause a leftward shift.

### B. Wave Equation and Solutions

Although electromagnetic waves generally have a vector amplitude, the scalar wave equation [33], [34] suffices for many radar problems including this one. Generally it can be expressed as

$$\nabla^2 s = \frac{1}{c^2} \frac{\partial^2 s}{\partial t^2}.$$

In one dimension this becomes

$$\frac{\partial^2 s}{\partial x^2} = \frac{1}{c^2} \frac{\partial^2 s}{\partial t^2}$$

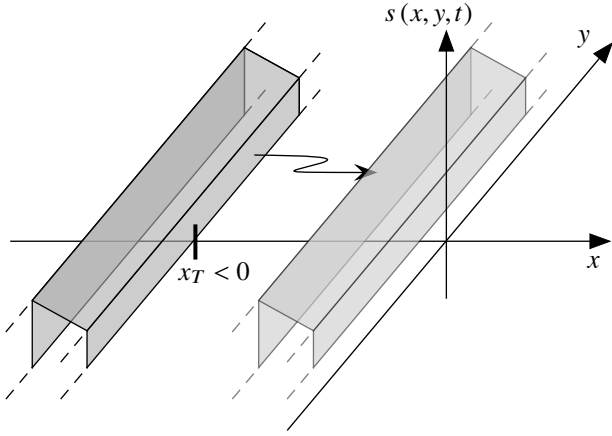


Fig. 3. Wave propagating to the right at the transmitter position  $x_T$  and at time  $t = 0$ .

and in three Cartesian dimensions it is

$$\frac{\partial^2 s}{\partial x^2} + \frac{\partial^2 s}{\partial y^2} + \frac{\partial^2 s}{\partial z^2} = \frac{1}{c^2} \frac{\partial^2 s}{\partial t^2}$$

with  $s$  the wave amplitude which is sometimes considered to be complex-valued;  $x$ ,  $y$ , and  $z$  are spatial coordinates,  $t$  is the time variable, and  $c$  is the constant propagation speed.

We start with a prototype function  $p(\cdot)$  and convert it into a traveling wave that satisfies a wave equation. In one dimension, two solutions are  $s(x, t) = p(\omega t - \kappa x + \phi)$  and  $s(x, t) = p(\omega t + \kappa x + \phi)^2$ . That these satisfy the wave equation can be shown by direct substitution as long as we constrain  $c = \omega/\kappa$ : in the first case,  $\partial s/\partial x = -\kappa p'$ ,  $\partial^2 s/\partial x^2 = \kappa^2 p''$ ,  $\partial s/\partial t = \omega p'$ ,  $\partial^2 s/\partial t^2 = \omega^2 p''$ . The former propagates in the  $+x$  direction and the latter in the  $-x$  direction as  $t$  increases according to the interpretation of II-A. The usefulness of having two constrained scale factors instead of just  $c$  will become apparent when we study monochromatic solutions in IV-B. We require a solution to exist in at least two spatial dimensions (the slant plane) as well as time. This is easily done, for a wave traveling in the  $+x$  direction, by simply defining the wave  $s$  as

$$s(x, y, t) = p(\omega t - \kappa x + \phi_s) \quad (1)$$

where  $\phi_s$  is to be determined. That  $y$  does not appear in the right-hand side of this expression simply expresses the fact that the wave amplitude does not depend on  $y$ , even though the wave exists in the  $(x, y)$  plane as it propagates—the wave value is constant as a function of  $y$ . This set-up will later allow waves propagating in other directions.

Assume that the radar is situated on the  $x$  axis at position  $x_T$  which is negative. See Fig. 3 for a rendering of a hypothetical prototype two-dimensional wave traveling to the right but just leaving the radar when  $t = 0$ . For simplicity, Fig. 4 displays Fig. 3 as viewed from the  $-y$  axis. We need to determine the term  $\phi_s$ . The figure shows the prototype  $p(x)$  in dashed form. We desire to scale  $p$  spatially by some amount to be determined so we include  $\kappa$ . We also include the time scale

<sup>2</sup>More traditional solutions are  $p(ct \pm x + \phi)$ . In the sequel, at least up to the point where monochromatic solutions are considered in IV-B, the reader might want to mentally substitute  $\omega = c$  and  $\kappa = 1$ .

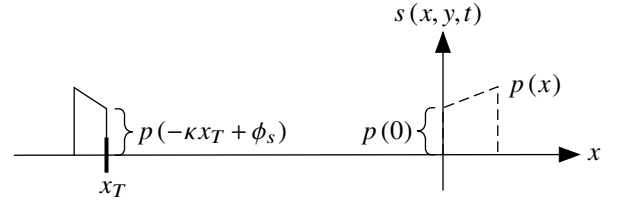


Fig. 4. Side view of a wave propagating to the right. The prototype wave is shown in dashed line.

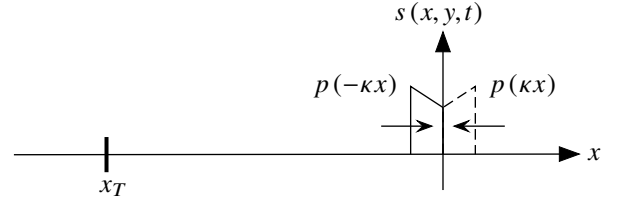


Fig. 5. A wave beginning the process of reflecting. The dashed form is the scaled prototype and from this point on can be considered to be the reflected wave for  $x < 0$ , traveling to the left.

factor  $\omega$ . Referring to the figure, we see that we need  $p$  to come out reversed, so that the leading edge in time is also the leading edge in space. This is because of the differing signs on the  $\omega t$  term and the  $\kappa x$  term in (1). With  $t = 0$  and  $x = x_T$  we write  $s(x_T, y, 0) = p(-\kappa x_T + \phi_s) = p(0)$ , resulting in  $\phi_s = \kappa x_T$  and

$$s(x, y, t) = p(\omega t - \kappa x + \kappa x_T).$$

Checking the result at  $t = 0$  we see that  $s(x, y, 0) = p(-\kappa(x - x_T))$ , flipped, scaled by  $\kappa$ , and shifted left by  $|x_T|$  since  $x_T$  is negative. This wave will propagate rightwards towards the origin for a time  $t_T$  where there is assumed to be a *point scatterer*, a small object which reflects part of the wave back towards the radar. (Later, point scatterers will be modeled as Dirac delta generalized functions.) Assuming for now that all of the wave's amplitude is reflected, we write  $s(x, y, t_T) = p(\omega t_T - \kappa x + \kappa x_T) = p(-\kappa x)$ , the latter requirement deriving from examining Fig. 5. Equating the arguments, we find that  $t_T = -x_T/c$ . This result could have been written by examination by knowing a little basic physics but here we have derived it fully.

### C. Field Due to One Scatterer

When  $t = t_T$ , a backward-traveling wave is created,  $r(x, y, t) = p(\omega t + \kappa x + \phi_r)$ . From Fig. 5 the requirements for a scatterer at  $x = 0$  are that

$$s(0, y, t_T) = r(0, y, t_T)$$

thus

$$p(\omega t_T + \kappa x_T) = p(\omega t_T + \phi_r)$$

leaving  $\phi_r = \kappa x_T$  and

$$r(x, y, t) = p(\omega t + \kappa x + \kappa x_T). \quad (2)$$

(Some function names will be recycled many times to mean different things so the actual meaning should be determined by the context of its use.) We can check a couple of cases. When

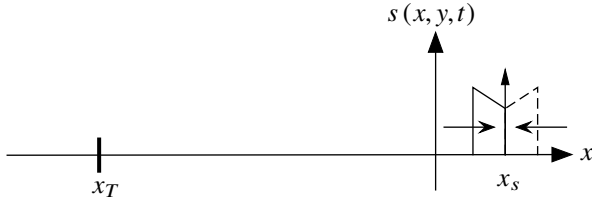


Fig. 6. A wave reflecting from a point scatterer at  $x_s$ .

$t = t_T$ ,  $r(x, y, t_T) = p[\kappa(x + x_T + ct_T)] = p(\kappa x)$  because  $ct_T = -x_T$ . Also,  $r(x, y, 0) = p[\kappa(x + x_T)]$ ; although it does not fit the physical model at times before the instant of reflection such as this one, the “pre-reflected” signal appears to the right of the central scatterer position. And back at the receiver,  $r(x, y, 2t_T) = p[\kappa(x - x_T)]$ ; as expected, the signal is about to enter the receiver. Similarly, the time waveform at the receiver can be found as  $r(x_T, y, t) = p[\omega(t - 2t_T)]$ , the original time waveform delayed by twice the one-way propagation time.

The above results can be generalized by allowing a scatterer that is not at the origin of the  $x$ - $y$  system. For a simple extension, let the scatterer be at  $(x, y) = (x_s, 0)$ . Using the same approach as before, the form of the reflected, backward-traveling wave is the same,  $r(x, y, t) = p(\omega t + \kappa x + \phi_r)$ , but now  $\phi_r$  will be different because the conditions have changed. The propagation speed  $c$  was found earlier as the proportionality between time and space so that now  $x_s = ct_s$ . Examining Fig. 6, apparently the required conditions are

$$s(x_s, y, t_T + t_s) = r(x_s, y, t_T + t_s)$$

thus

$$p(\omega t_T + \omega t_s - \kappa x_s + \kappa x_T) = p(\omega t_T + \omega t_s + \kappa x_s + \phi_r)$$

resulting in  $\phi_r = \kappa(x_T - 2x_s)$  and

$$r(x, y, t) = p[\omega t + \kappa(x + x_T - 2x_s)].$$

When  $t = t_T + 2t_s$ ,  $r(x, y, t_T + 2t_s) = p(\kappa x)$ ; the reflected wave has progressed back to the origin, the forward wave taking  $t_T + t_s$  seconds to travel to the scatterer plus an additional  $t_s$  seconds to reflect back to the origin. Perhaps more interesting,  $r(x, y, 2t_T) = p[\kappa(x - x_T - 2x_s)]$ , that is, the “bulk delay” of  $2t_T$  having elapsed, the signal is  $2x_s$  spatial units in front of the receiver. This mental picture of the spatial signal or several different copies of it “stacked up” in front of the receiver will be useful later. In double the total round-trip travel time,  $r(x, y, 2t_T + 2t_s) = p[\kappa(x - x_T)]$  and the wave is back at the receiver.

A further generalization is shown in Fig. 7 which is once again displayed as an  $x$ - $y$  plane but with an overhead view. Here, a scatterer is shown at position  $\mathbf{r}_s = (x_s, y_s)$ . Since the wave is planar and its wavefront is perpendicular to the  $x$  axis, it reflects from the scatterer at the same time as a scatterer at  $(x_s, 0)$ <sup>3</sup>, so the previous result applies, as we insert the geometrical form for  $x_s$ ;

$$r(x, y, t) = p[\omega t + \kappa(x + x_T - 2|\mathbf{r}_s| \cos \theta_s)].$$

<sup>3</sup>This is the crux of the plane wave approximation. With a spherical wave, this point would reflect later than a point on the  $x$  axis at the same  $x_s$  distance.

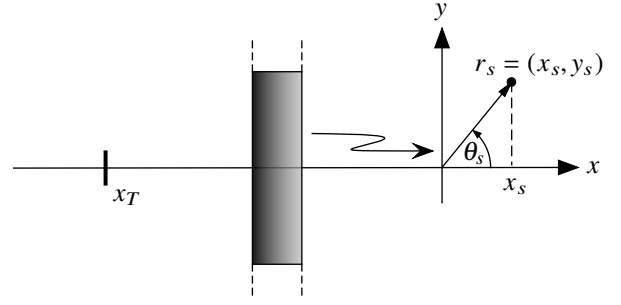


Fig. 7. A propagating wave approaching a point scatterer off the  $x$  axis, at  $r_s$ .

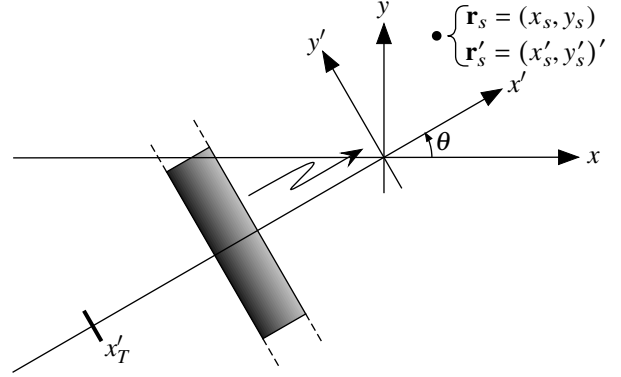


Fig. 8. Coordinates  $(x', y')$  rotated  $\theta$  with the radar at  $-x'_T$ .

Yet another generalization for the propagation model will be to consider waves traveling not parallel to the  $x$  axis but at an angle  $\theta$  relative to the  $x$  axis. Fig. 8 shows this situation, employing a coordinate system  $(x', y')$  which is rotated by an angle  $\theta$  relative to the  $(x, y)$  coordinates. Concerning notation, the prime mark  $'$  will be used on rotated coordinate variables, functions associated with those variables, and when denoting coordinate pairs in the rotated system,  $(\cdot, \cdot)'$ . Unless stated otherwise there will always be the assumption of a rotation by an angle  $\theta$ . For a radar at  $(x'_T, 0)'$  and a scatterer at  $(x'_s, 0)'$ , the situation is the same as the non-rotated system so we can immediately write

$$r'(x', y', t) = p[\omega t + \kappa(x' + x'_T - 2x'_s)]. \quad (3)$$

Before proceeding with this more useful case, first consider the simplified system where  $r'(x', y', t) = p[\omega t + \kappa x']$ . The rotated coordinates, in terms of the unrotated coordinates, are

$$\begin{aligned} x' &= x \cos \theta + y \sin \theta \\ y' &= -y \sin \theta + x \cos \theta \end{aligned} \quad (4)$$

so that the simplified wave expressed in the  $x$ - $y$  coordinates is

$$r(x, y, t) = p[\omega t + \kappa(x \cos \theta + y \sin \theta)]. \quad (5)$$

Let  $\mathbf{r} = (x, y)$  be a generic point in the  $x$ - $y$  system and define a vector<sup>4</sup>  $\boldsymbol{\kappa} = (\kappa \cos \theta, \kappa \sin \theta) = (\kappa_x, \kappa_y)$  denoting a wave

<sup>4</sup>As we introduce vectors and dot products, recall that a convenient property of non-zero vectors  $\mathbf{a}$  and  $\mathbf{b}$  is that  $\mathbf{a} \cdot \mathbf{b} = |\mathbf{a}| |\mathbf{b}| \cos \alpha$  where  $\alpha$  is the included angle.

traveling in the  $\theta$  direction with scale factor  $\kappa = |\boldsymbol{\kappa}|$ . Now the generic, simplified wave (5) can be expressed as

$$r(x, y, t) = p(\omega t + \boldsymbol{\kappa} \cdot \mathbf{r}). \quad (6)$$

But instead of this simplified set-up we have (3) in which  $x'_T$  and  $x'_s$  are also expressible using forms similar to (4). Assuming the notation

$$\begin{aligned} \mathbf{r} &= (x, y) & \mathbf{r}_T &= (x_T, y_T) & \mathbf{r}_s &= (x_s, y_s) \\ \mathbf{r}' &= (x', y')' & \mathbf{r}'_T &= (x'_T, y'_T)' & \mathbf{r}'_s &= (x'_s, y'_s)' \end{aligned}$$

for respectively a generic point, the transmitter location, and a scatterer location in each of the coordinate systems, we can use the same process above to get the compact representation for the wave reflected from a point scatterer on the  $x'$  axis:

$$r(x, y, t) = p[\omega t + \boldsymbol{\kappa} \cdot (\mathbf{r} + \mathbf{r}_T - 2\mathbf{r}_s)].$$

This result deserves two notes. First, we defined  $\mathbf{r}'_s = (x'_s, y'_s)'$ , not  $\mathbf{r}'_s = (x'_s, 0)'$ , that is, the scatterer was not constrained to lie on the  $x'$  axis and so the result is more general. The quantity  $\boldsymbol{\kappa} \cdot \mathbf{r}'_s = \text{constant}$  defines a line of constant wave amplitude that is perpendicular to the  $x'$  axis. All reflections from reflectors that lie on this line return to the receiver at the same time. Second, the receiver in practice will start recording only around the time that the signal of interest, reflected from the ground patch, arrives. There is no purpose to recording sooner than that because there will be little or no reflected signal or the reflected signal that might exist will be of no interest. In practice there will be many scatterers or a continuum of scatterers and the receiver will begin recording only when the earliest reflection of interest arrives. We have seen that the round-trip delay from a scatterer at the center of the coordinate systems is  $2t_T = -2x_T/c$ .  $x_T$  is now seen as a rather arbitrary reference point for the wave and is not necessarily the most useful reference since it describes a lot of delay that doesn't carry any information since it is common to all transmitted pulses. Therefore, we will eliminate it, or rather, set it to zero, as doing this better models the receiver at around the time that it is recording the signal of interest. (More precisely, we are shifting the data by this much.) We note that setting it to zero along with the likelihood that the center of the coordinate systems will be the center of the ground patch will result in a non-causal signal. This is not a problem if we consider that we are ultimately desiring to reconstruct an image of the ground reflectivity and as such, non-causality for spatial signals is not an existential question as it is for temporal signals. In the latter case, the reference can be explicitly adjusted to avoid the problem or, more practically, the way that an array in computer memory is interpreted can simply be modified. Thus, the expression for the reflected wave field can be written

$$r(x, y, t) = p[\omega t + \boldsymbol{\kappa} \cdot (\mathbf{r} - 2\mathbf{r}_s)] \quad (7)$$

If  $\mathbf{r}_s = (0, 0)$ , i.e. if the scatterer is at the origin, then we get back the familiar form  $r(x, y, t) = p(\omega t + \boldsymbol{\kappa} \cdot \mathbf{r})$  and if  $\boldsymbol{\kappa} = (\kappa, 0)$  then we get back the earlier familiar form  $r(x, y, t) = p(\omega t + \kappa x)$  since  $(\kappa, 0) \cdot (x, y) = \kappa x$ .

### III. THE RECEIVER SIGNAL

The previous work has derived the field due to a radar signal reflection from a single scatterer. There remain more tasks: find the signal that is actually recorded by the radar receiver, show how to form—reconstruct, in radar terminology—the image of a single scatterer, and show how to form the image of an actual ground patch that consists of more than a single point scatterer.

#### A. Point Scatterers

The radar receiver does not record the entire field  $r(x, y, t)$  or  $r'(x', y', t)'$  but only a slice or sample of that field, per each transmission of  $p(\cdot)$ . For a monostatic radar that sample is  $r'(x', 0, t)'$ —the  $y'$  aspect has been lost, having been sampled at a single  $y'$  location,  $y' = 0$ . Samples from different angles are recorded for different orientations of the  $x'$ - $y'$  system, that is, for different  $\theta$ , and the various recorded signals are processed as a group to form the ground patch image. The sampled or sliced return  $r'(x', 0, t)'$  is a function only of a single spatial variable and time and these variables are linked by the propagating nature of the wave, namely, by the propagation speed  $c$ . In what follows both a time-domain version and a space-domain version of the receiver signal will be allowed, and these are notated respectively  $r'_t(\cdot)$  and  $r'_x(\cdot)$  where the latter subscript is intended to denote “space” and not a particular coordinate system.

Examining first the case of a point scatterer on the  $x'$  axis, the result (3) can be readily converted to both a temporal and a spatial receiver function. To get the time function at the receiver, fix the spatial variable to be at the receiver by letting  $x' = x'_T$ ; then  $r'(x'_T, 0, t) = p[\omega t + \kappa(2x'_T - 2x'_s)]$ . With  $x_s = ct_s$  and  $x_T = -ct_T$ ,  $r'(x'_T, 0, t) = p[\omega(t - 2t_T - 2t_s)]$ . Setting the phase reference to zero as before and adopting the receiver signal notation for time domain, then

$$r'_t(t) = p[\omega(t - 2t_s)]. \quad (8)$$

The time signal is delayed by the amount of delay coded in the position of the scatterer relative to the  $x'$ - $y'$  system.

Next, examine the case of the point scatterer at the same position but derive the spatial signal at the receiver. Since we are hoping to eventually constitute a spatial picture, this is potentially a more useful function. It is helpful to imagine the reflected signal at  $t = 2t_T$  as frozen in time, somewhere in the vicinity of the receiver. Substituting  $t = 2t_T$  into (3),  $r'(x', 0, 2t_T) = p(2\omega t_T + \kappa x' + \kappa x'_T - 2\kappa x'_s)$ . Recalling that  $t_T = -x_T/c$ , we get  $r'(x', 0, 2t_T) = p[\kappa(x' - x'_T - 2x'_s)]$  and we see that the signal is  $2x_s$  spatial units in front of the receiver, the factor two appearing because two-way travel doubles the distance. Finally, using the zeroed phase reference and invoking the one-dimensional spatial signal notation,

$$r'_x(x') = p[\kappa(x' - 2x'_s)]. \quad (9)$$

By now we recognize that some “ $\omega t$ ” quantities can be replaced with “ $\kappa x$ ” quantities and we could have arrived at (9) more directly with this replacement in (8).

To get the receiver signal for a scatterer located off the rotated  $x'$  axis, consider Fig. 9 in particular  $\mathbf{r}_s$ . Let  $\hat{x}'$  be a

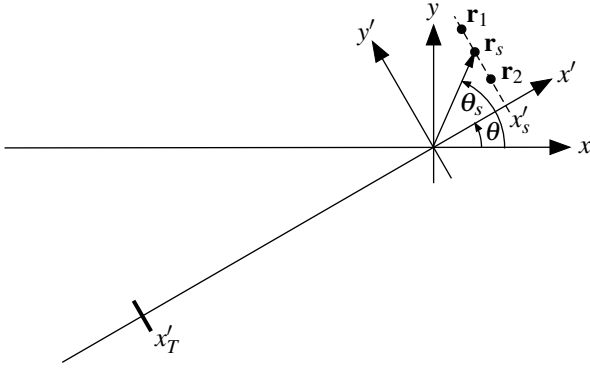


Fig. 9. Scatterers perpendicular to the wave direction are reflected at the same time.

unit vector pointing in the direction of the  $x'$  axis at angle  $\theta$  relative to the  $x$  axis,  $\hat{\mathbf{x}}' = (\cos \theta, \sin \theta)$ . Then  $x'_s = \hat{\mathbf{x}}' \cdot \mathbf{r}_s = |\mathbf{r}_s| \cos(\theta_s - \theta)$ . The scaled- $x'$  units accumulated from the origin to  $x'_s$  is  $\kappa x'_s = |\kappa| |\mathbf{r}_s| \cos(\theta_s - \theta) = \kappa \cdot \mathbf{r}_s$  and thus, recalling (9),

$$r'_x(x') = p(\kappa x' - 2\kappa \cdot \mathbf{r}_s). \quad (10)$$

### B. Multiple and Continuous Scatterers

We now turn to having multiple point scatterers and then a continuously reflecting ground patch. Considering again Fig. 9, let there be multiple scatterers that happen to lie along the line  $\hat{\mathbf{x}}' \cdot \mathbf{r}_s = x'_s$ , call them  $\{\mathbf{r}_n\}_{n=1}^{N_s}$ . Then by construction,

$$\hat{\mathbf{x}}' \cdot \mathbf{r}_1 = \hat{\mathbf{x}}' \cdot \mathbf{r}_2 = \dots = \hat{\mathbf{x}}' \cdot \mathbf{r}_{N_s} = \hat{\mathbf{x}}' \cdot \mathbf{r}_s$$

and also

$$\kappa \cdot \mathbf{r}_1 = \kappa \cdot \mathbf{r}_2 = \dots = \kappa \cdot \mathbf{r}_{N_s} = \kappa \cdot \mathbf{r}_s.$$

Each reflects  $p(\cdot)$  with its own weight or reflection coefficient,  $\{\gamma_n\}_{n=1}^{N_s}$ , and each reflected  $\gamma_n p(\cdot)$  adds to the others<sup>5</sup>. The reflection coefficients  $\gamma_n$  are complex-valued to allow for both amplitude and phase modification of the reflected signal. Assuming linearity, the receiver signal due to all the reflections is

$$r'_x(x') = p(\kappa x' - 2\kappa \cdot \mathbf{r}_s) \sum_{n=1}^{N_s} \gamma_n. \quad (11)$$

If there is instead a continuum of reflectors  $\gamma(y')$  along the same line then the receiver signal takes the form

$$r'_x(x') = p(\kappa x' - 2\kappa \cdot \mathbf{r}_s) \int \gamma(y') dy' \quad (12)$$

where the integration limits are usually considered to be set by the ground patch as it is illuminated by the main beam of the antenna.

Now consider a ground patch which is comprised of a series of reflectors arranged along the  $x'$  axis, as shown in Fig. 10.

<sup>5</sup>There are two assumptions at work here. The first is linearity, that reflections sum in proportion to the reflection coefficients. The second is the Born approximation which assumes that secondary reflections between scatterers are weak and can be ignored. This is potentially a severe limitation of SAR in some situations and it is rarely addressed. An exception is [35] in imaging the interiors of comets.

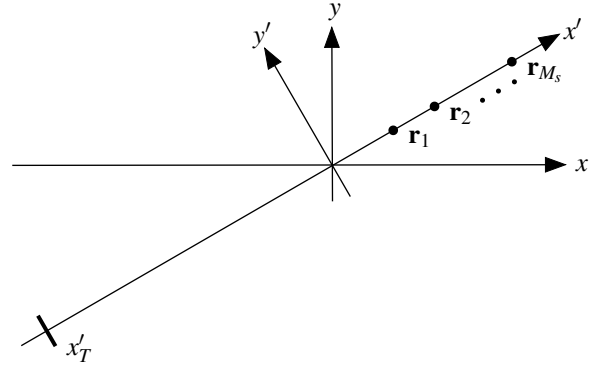


Fig. 10. Multiple scatterers aligned on the  $x'$  axis

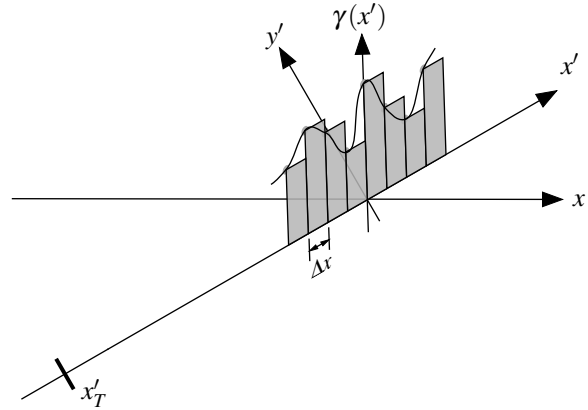


Fig. 11. A continuous one-dimensional scattering function  $\gamma(x')$  in the  $x'$  direction quantized by  $\Delta x$ .

Let the scatterers be  $\{\mathbf{r}_m\}_{m=1}^{M_s}$  such that each  $\mathbf{r}_m = (x'_m, 0)'$  and again associate a set of reflection coefficients  $\{\gamma_m\}_{m=1}^{M_s}$ . From (9) and the assumption of linearity, the receiver signal is

$$r'_x(x') = \sum_{m=1}^{M_s} \gamma_m p[\kappa(x' - 2x'_m)].$$

An important difference with (11) is that here, copies of  $p(\cdot)$  arrive at different times due to scatterers being different distances from the receiver and thus must therefore appear under the summation. In order to pass to a continuous distribution of scatterers along  $x'$ , Fig. 11 shows a division of the axis approximating a continuous reflectivity  $\gamma(x')$  as a series of  $M$  equal-width rectangles according to a standard method of calculus. Allowing for a dummy variable  $\xi$  under the summation results in

$$r'_x(x') \approx \sum_{m=0}^{M-1} \gamma(m \Delta \xi) p(\kappa x' - 2\kappa m \Delta \xi) \Delta \xi.$$

As  $M \rightarrow \infty$  and  $\Delta \xi \rightarrow 0$  we get the integral

$$r'_x(x') = \int \gamma(\xi) p[\kappa(x' - 2\xi)] d\xi. \quad (13)$$

We would now like to combine the results (12) and (13). Towards this end introduce a general *ground patch*  $g(x, y)$  illuminated by the antenna. Recall the earlier discussion of the slant plane and that the ground patch as used here is the

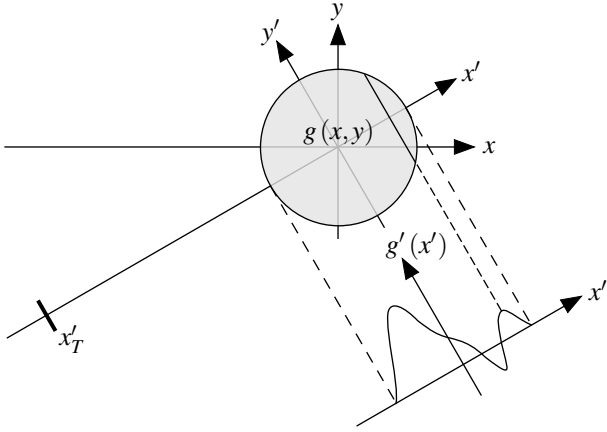


Fig. 12. A projection  $g'(x')$  as a collection of line integrals through a ground patch  $g(x, y)$  at an angle  $\theta$ .

actual area on the ground that is illuminated, projected onto a plane containing the radar and the center of the actual ground patch. (12) contains continuous scatterers that were artificially constrained to lie on a line parallel to the  $y'$  axis and an integration was calculated along this line. With  $g(x, y)$ , this operation properly becomes a line integral along the same line but cutting through the ground patch. This line integral can be expressed in several ways, including [36], by solving (4) for  $x$  and  $y$ ,

$$g'(x') = \int g(x' \cos \theta - y' \sin \theta, x' \sin \theta + y' \cos \theta) dy'$$

and [20]

$$g'(x') = \iint g(x, y) \delta(x' - \hat{\mathbf{x}}' \cdot \mathbf{x}) dx dy$$

or more compactly,

$$g'(x') = \int g(\mathbf{x}) \delta(x' - \hat{\mathbf{x}}' \cdot \mathbf{x}) d\mathbf{x} \quad (14)$$

where  $\delta(\cdot)$  is the one-dimensional Dirac delta generalized function or simply one-dimensional impulse. Both of these express the fact that scatterers on a line parallel to the  $y'$  axis arrive back at the receiver at the same time. In applications, this set of line integrals through the ground patch is called a *projection of  $g(x, y)$  at angle  $\theta$*  or  $\theta$ -*projection* as shown in Fig. 12. Generally, this function evaluated over all  $\theta$  and perhaps more clearly denoted with the redundant—in our notation— $g'(\theta, x')$ , is known as the *Radon transform* of  $g(x, y)$ <sup>6</sup>. Despite the appearance of a function of polar coordinates— $x'$  in radius and  $\theta$  in angle—this function should not be considered as an expression in polar coordinates because it is multi-valued at  $x' = 0$ . It is, however, periodic in  $\theta$  with period  $2\pi$ . Examples of Radon transforms computed from a simple test function can be found in [20] and [27] among many other places. With this understanding of  $g'(x')$  and in view of (13), we can replace the integration of the continuous line of

<sup>6</sup>The Radon transform is closely related to the Hough transform which is used to detect shapes, commonly lines, in digital images [20], [37]. In SAR, the Radon transform is of the ground patch which is not digital.

scatterers along the  $x'$  axis  $\gamma(\xi)$  with the line integral  $g'(x')$  and write

$$r'_x(x') = \int g'(\xi) p[\kappa(x' - 2\xi)] d\xi = r'_x(\theta, x'). \quad (15)$$

To recap: this is the spatial version of the signal at the receiver for a general ground patch  $g(x, y)$  after adjusting the phase reference  $x_T = 0$ .  $g'(x')$  is the projection, a set of line integrals through  $g(x, y)$  at angle  $\theta$ . The received signal is the convolution of a possibly scaled version of the basic signal with the projection of the ground patch. This result compares to a central result of [1] wherein a mixed spatial-temporal signal format is preferred.

To demonstrate the use of (15), consider again the receiver response to an off-center scatterer when the radar is on the  $\theta$ -rotated  $x'$ - $y'$  system. The scatterer is modeled as an impulse at  $\mathbf{r}_s$ , that is,  $g(x, y) = \delta_2(\mathbf{x} - \mathbf{r}_s)$  where  $\delta_2(\cdot)$  is the two-dimensional Dirac delta generalized function or simply the two-dimensional impulse. If  $\mathbf{r}_s = (x_s, y_s)$ , then  $g(x, y) = \delta_2(\mathbf{x} - \mathbf{r}_s) = \delta(x - x_s) \delta(y - y_s)$ . The projection of the ground patch is  $g'(x') = g'(\theta, x') = \delta(x' - x'_s) = \delta(x' - \hat{\mathbf{x}}' \cdot \mathbf{r}_s) = \delta(x' - |\mathbf{r}_s| \cos(\theta - \theta_s))$ . This Radon transform of the off-center two-dimensional impulse is an impulsive ridge tracing a sinusoidal pattern in the  $\theta$ - $x'$  Radon plane with  $x'$ -amplitude  $|\mathbf{r}_s|$  and phase  $\theta_s$ . In a more complicated ground patch the Radon transform plotted this way will appear to have many sinusoidal patterns of various intensities (height of ridge or other feature), amplitudes in  $x'$ , and phases in  $\theta$  superimposed; for this reason such graphical displays are sometimes called *sinograms*. Placing this into (15) gives

$$r'_x(x') = \int \delta(\xi - \hat{\mathbf{x}}' \cdot \mathbf{r}_s) p[\kappa(x' - 2\xi)] d\xi$$

which evaluates to

$$r'_x(x') = p[\kappa(x' - 2\hat{\mathbf{x}}' \cdot \mathbf{r}_s)] = p(\kappa x' - 2\kappa \cdot \mathbf{r}_s) \quad (16)$$

which is reassuringly the same as (10). For a centered scatterer,  $\mathbf{r}_s = (0, 0)'$ , the result is just

$$r'_x(x') = p(\kappa x').$$

#### IV. IMAGE RECONSTRUCTION

We now specialize  $p(\cdot)$  to a particular form, introduce two-dimensional Fourier transforms, and show how one or more scatterers—impulses in the ground patch—can be reconstructed from several  $r'_x(x')$  as measured from different  $\theta$ s.

##### A. Wave Notation

So far, the form of  $p(\cdot)$  has been completely general, unspecified. In the development it has been portrayed graphically as a generic pulse but that was only for convenience and to allow us to think of a “leading edge” as a time reference. In fact, any other feature of any other signal could have served as a time reference. Indeed, there has been so far no functional limitation on  $p(\cdot)$  whatsoever.

Before we proceed further we need to introduce a bit of new notation. Up to now we have used  $\kappa$  as a scale factor in a generic, prototype function, and a vector version  $\boldsymbol{\kappa}$  that

connotes both a scale factor and a direction of propagation. As useful as this is, we will introduce a new vector which will subsume  $\kappa$  if we want it to. With  $k$  real, define a new vector  $\mathbf{k} = k\kappa$  so that  $|\mathbf{k}| = |k| |\kappa|$  and so that  $\mathbf{k}$  points in the same or opposite direction as  $\kappa$  depending on the sign of  $k$ . This set-up provides a two-level scaling for the spatial aspect of the wave, a convenience in some cases but a nuisance in others. Therefore, consider a usage whereby  $\kappa$  is a unit vector,  $\kappa = 1$ , and thus  $|\mathbf{k}| = |k|$ . This effectively disables the scaling due to  $\kappa$  for instances where  $p(\cdot)$  requires no scaling but leaves it as an option when needed while offering a standard wave notation for what follows. That  $|\kappa| = 1$  will bear on everything we do in the sequel unless stated otherwise. An effect of this choice is that (15) simplifies a little:

$$\begin{aligned} r'_x(x') &= \int g'(\xi) p(x' - 2\xi) d\xi = r'_x(\theta, x') \\ &= g'(x') * p(2x') \end{aligned} \quad (17)$$

where the second line expresses the relationship with convolution notation. An alternate form of (17), found by changing variables under the integral, is

$$r'_x(x') = \frac{1}{2} \int g' \left( \frac{\xi}{2} \right) p(x' - \xi) d\xi$$

which can ease computations in some cases<sup>7</sup>. Notably, for a particular angle  $\theta$ , if  $p(\cdot)$  is an impulse, the projection of the ground patch at angle  $\theta$  is returned directly as the receiver signal but with a scaling by 1/2 in amplitude and distance—stretched in space. Alternately, if the ground path  $g(\mathbf{x}) = \delta_2(\mathbf{x})$ , the transmitted pulse is returned directly,  $r'_x(x') = p(x')$  as we have seen earlier. Otherwise, the scaled projection is filtered by a filter which has an impulse response of  $p(x)$ .

## B. Monochromatic Waves

Now, consider a specific form for  $p(\cdot)$ , a monochromatic (“one color”) plane wave, the two-dimensional traveling wave spatial analog of a sinusoidal function of time. The desired form is<sup>8</sup>

$$p(\omega t - kx) = e^{j(\omega t - kx)}.$$

The right-hand side is a periodic function of its argument. For example, hold  $x$  constant and consider a time-based phase function  $\phi_t(t) = \omega t$ . Define  $T$  such that  $\phi_t(t + T) = \phi_t(t) + 2\pi = \omega(t + T)$  implying that the period  $T = 2\pi/\omega$ . Similarly define a space-based phase function  $\phi_x(x) = kx$  while holding  $t$  constant. Then define  $\lambda$  such that  $\phi_x(x + \lambda) = \phi_x(x) + 2\pi$ , implying that  $\lambda = 2\pi/k$ ;  $\lambda$ , the spatial period, is called the *wavelength*. For a scatterer at  $\mathbf{r}_s$ , from (7), the reflected field is

$$r(x, y, t) = e^{j[\omega t + \mathbf{k} \cdot (\mathbf{r} - 2\mathbf{r}_s)]} = e^{j[\omega t + k_x(x - 2x_s) + k_y(y - 2y_s)]} \quad (18)$$

<sup>7</sup>Care should be taken when computing with delta generalized functions. For example,  $\delta(x/2) = 2\delta(x)$  which result is found by writing the delta as its defining limiting integral and changing variables.

<sup>8</sup>Obviously a radar signal has to have a beginning and an ending, a pulse. Here we shall push that detail aside for the time being and revisit it later in this section.

which, as set up before, propagates backwards along the  $x'$  axis which is rotated from the  $x$  axis by  $\theta$ . The *wavenumber vector* is  $\mathbf{k} = (k \cos \theta, k \sin \theta) = (k_x, k_y)$  with  $k = |\mathbf{k}|$  and indicates the direction opposite the direction of propagation;  $k$  is the *wavenumber* or *spatial frequency* in radians/m along the  $x'$  axis, and  $k_x$  and  $k_y$  are the wavenumbers in the  $x$  and  $y$  directions respectively. For example, if  $\theta = 0$ , then  $k_x = k$  and  $k_y = 0$ ; there is no spatial variation in the  $y$  direction.  $\omega$  is the temporal frequency in radians/s and as stated earlier the propagation speed is implied by the relationship  $c = \omega/k$ . The monochromatic receiver signal from a scatterer, from either (10) or (16), is

$$r'_x(x') = e^{j(kx' - 2\mathbf{k} \cdot \mathbf{r}_s)}. \quad (19)$$

If the scatterer  $\mathbf{r}_s$  is at the origin then the previous two equations become, for the field,

$$r(x, y, t) = e^{j(\omega t + \mathbf{k} \cdot \mathbf{r})} \quad (20)$$

and

$$r'_x(x') = e^{jkx'} \quad (21)$$

for the receiver signal.

## C. Fourier Transforms

The two-dimensional Fourier transform and its inverse with space and wavenumber as the conjugate variables are, in the traditional analysis and synthesis interpretations respectively,

$$S(k_x, k_y) = \iint s(x, y) e^{-j(k_x x + k_y y)} dx dy$$

and

$$s(x, y) = \frac{1}{4\pi^2} \iint S(k_x, k_y) e^{j(k_x x + k_y y)} dk_x dk_y \quad (22)$$

where the limits of integration are assumed to be from  $-\infty$  to  $\infty$  unless stated otherwise for some special case. (This  $s$  is different than the  $s$  of II-B.) A more compact notation suitable for any number of dimensions is

$$S(\mathbf{k}) = \int s(\mathbf{x}) e^{-j\mathbf{k} \cdot \mathbf{x}} d\mathbf{x}$$

and

$$s(\mathbf{x}) = \frac{1}{(2\pi)^n} \int S(\mathbf{k}) e^{j\mathbf{k} \cdot \mathbf{x}} d\mathbf{k}$$

where the multiplicity of the integrals  $n$  is the same as the dimensionality of the vectors. When  $n = 2$  or  $n = 3$ ,  $S(\mathbf{k})$  is sometimes called the *plane wave spectrum* or *angular spectrum* of the field  $s(\mathbf{x})$ . In the above, we have used the convention that lower-case and upper-case versions of the same letter symbol represent Fourier transform pairs, i.e.,  $S(\mathbf{k}) = \mathcal{F}\{s(\mathbf{x})\}$  with  $\mathcal{F}\{\cdot\}$  representing the Fourier transform operator. These transform definitions could be increased in dimensionality by one by including the time component since all of the basic functional forms that we have dealt with include an  $\omega t$  component of the argument [38]. However, we have eliminated this factor in the receiver signal by freezing time at  $t = 2t_T$ . For the general field for monochromatic waves such as (18), it is common practice by most authors to remove, cancel, or simply

ignore the  $e^{j\omega t}$  term. In the first case, the remaining spatial term is called a *phasor*, indicating the complex amplitude of the  $\omega$ -oscillating field at each position  $(x, y)$ . The phasor concept is common in circuit theory but works just as well here. In the second case, ignoring the time term, some authors simply state that the time component is “understood”; the difference is really one of style but it seems more satisfying to specify the phasor concept. It is in this way that the two-dimensional spatial transform works for these monochromatic field problems.

With the Fourier transform now defined it is possible to state the Fourier transforms of (15) and (17) which will be useful soon. The Fourier transform of the doubly-scaled (15) with respect to  $x'$  is

$$R'_x(k) = \frac{1}{\kappa} G'(2k) P\left(\frac{k}{\kappa}\right) = R'_x(\theta, k) \quad (23)$$

whereas the Fourier transform of the simplified version (17) is

$$R'_x(k) = G'(2k) P(k) = R'_x(\theta, k). \quad (24)$$

Two transforms will be particularly useful. Consider first the Fourier transform of an impulse at  $\mathbf{x}_0$ ,

$$\mathcal{F}\{\delta(\mathbf{x} - \mathbf{x}_0)\} = \int \delta(\mathbf{x} - \mathbf{x}_0) e^{-j\mathbf{k}\cdot\mathbf{x}} d\mathbf{x} = e^{-j\mathbf{k}\cdot\mathbf{x}_0},$$

which is a stationary plane-wave-like function in the wavenumber domain oriented at an angle equal to the angle between the vector  $\mathbf{x}_0$  and the  $x$  axis, with period in that same direction of  $2\pi/|\mathbf{x}_0|$ . Also,

$$\mathcal{F}^{-1}\{e^{-j\mathbf{k}\cdot\mathbf{x}_0}\} = \frac{1}{4\pi^2} \int e^{j\mathbf{k}\cdot(\mathbf{x}-\mathbf{x}_0)} d\mathbf{k} = \delta(\mathbf{x} - \mathbf{x}_0). \quad (25)$$

If the impulse is centered,  $\mathbf{x}_0 = (0, 0)$ , then

$$\mathcal{F}\{\delta(\mathbf{x})\} = 1$$

and then the trivial but important result, for our purposes,

$$\mathcal{F}^{-1}\{1\} = \frac{1}{4\pi^2} \int 1 \cdot e^{j\mathbf{k}\cdot\mathbf{x}} d\mathbf{k} = \delta(\mathbf{x}). \quad (26)$$

This well-known transform says that *an impulse can be constructed by summing equal-amplitude plane waves of all wavenumbers and all orientations*. Of course it is impossible to collect this much data from any system. We shall take the position that any amount of data will provide some sort of useful result and as such we consider measuring or sampling parts of the wavenumber domain. Thinking in the  $k_x$ - $k_y$  plane, one can imagine, for example, measuring some rectangular region  $k_{x1} \leq k_x \leq k_{x2}$  and  $k_{y1} \leq k_y \leq k_{y2}$  or an annular region  $k_{\min} \leq k \leq k_{\max}$  or a collection of impulses  $\{\delta(\mathbf{k} - \mathbf{k}_i)\}_{i=1}^I$ . As is well known and as we shall see soon, spotlight SAR collects data from a truncated annulus defined by  $k_{\min} \leq k \leq k_{\max}$  and  $\theta_{\min} \leq \theta \leq \theta_{\max}$ . The  $\theta$ -variation is obtained by moving the radar around the ground patch and the  $|\mathbf{k}|$  variation is obtained by producing signals with a range of frequencies in  $\omega$ .

For the second useful transform, we show simply the Fourier transform of a plane wave  $e^{j\mathbf{k}_0\cdot\mathbf{x}}$  so that

$$\mathcal{F}\{e^{j\mathbf{k}_0\cdot\mathbf{x}}\} = \int e^{-j(\mathbf{k}-\mathbf{k}_0)\cdot\mathbf{x}} d\mathbf{x} = \delta(\mathbf{k} - \mathbf{k}_0). \quad (27)$$

Thus, a plane wave with wavenumber vector  $\mathbf{k}_0$  is expressed simply in the wavenumber domain as  $\delta(\mathbf{k} - \mathbf{k}_0)$ .

#### D. Projections and Slices

We now have the pieces we need to derive an important result. Compute the one-dimensional Fourier transform of the projection (14):

$$\mathcal{F}\{g'(x')\} = G'(k) = \int g'(x') e^{-jkx'} dx'.$$

Substitute (14) and reverse the order of integration,

$$\begin{aligned} G'(k) &= \iint g(\mathbf{x}) \delta(x' - \hat{\mathbf{x}}' \cdot \mathbf{x}) e^{-jkx'} d\mathbf{x} dx' \\ &= \int g(\mathbf{x}) e^{-jk\hat{\mathbf{x}}' \cdot \mathbf{x}} d\mathbf{x} \\ &= G(k\hat{\mathbf{x}}') \\ &= G(k \cos \theta, k \sin \theta) \\ &= G(k_x, k_y) \\ &= G(\mathbf{k}) \end{aligned}$$

where  $G(\mathbf{k})$  is the two-dimensional Fourier transform of the ground patch reflectivity  $g(\mathbf{x})$ . The salient version, for our purposes, is

$$G'(k) = G(k\hat{\mathbf{x}}') \quad (28)$$

which is often referred to as the Projection Slice Theorem. It states that the one-dimensional Fourier transform of a  $\theta$ -projection is the same as a *slice at angle*  $\theta$  through the origin of the two-dimensional Fourier transform of the ground patch reflectivity. Even though the argument of the the right-hand side of (28) accesses the  $\mathbf{k}$ -plane generally, the notation  $G(k\hat{\mathbf{x}}')$  allows a convenient parameterization in polar coordinates with the radius expressed as  $k$  and the angle  $\theta$  expressed within the unit vector  $\hat{\mathbf{x}}' = (\cos \theta, \sin \theta)$ .

This result contains nothing of the transmitted signal. But this was worked out earlier in (24) so now we can also write

$$R'_x(k) = G(2k\hat{\mathbf{x}}') P(k) = R'_x(\theta, k) \quad (29)$$

and, at least in principle, we can recover the effect of a transmitted signal that has a non-flat spectrum as

$$G(2k\hat{\mathbf{x}}') = \frac{R'_x(k)}{P(k)}.$$

Divisions of this sort must always be done cautiously; obviously it will fail where  $P(k) = 0$ . One should also expect failure when  $P(k)$  is small due to noise spoiling the calculation. And one should never divide by a spectrum calculated by a discrete Fourier transform (DFT) without first taking steps to deal with the periodicity; to see what the problem is, calculate and plot the inverse DFT of the reciprocal of the discrete Fourier transform without zero padding—this is what is being convolved with  $R'_x(k)$ . There are methods of dealing with this deconvolution problem but they will not enter here. Some signals with approximately flat spectra include the linear frequency modulation (LFM) pulse, the windowed sinc pulse, and any sufficiently short pulse even though the latter can be expected to suffer from poor signal to noise ratio except possibly at short ranges—that is why LFM and pulse compression were developed for radar. As always, the bandwidth of  $R'_x(k)$  is inversely proportional to range resolution.

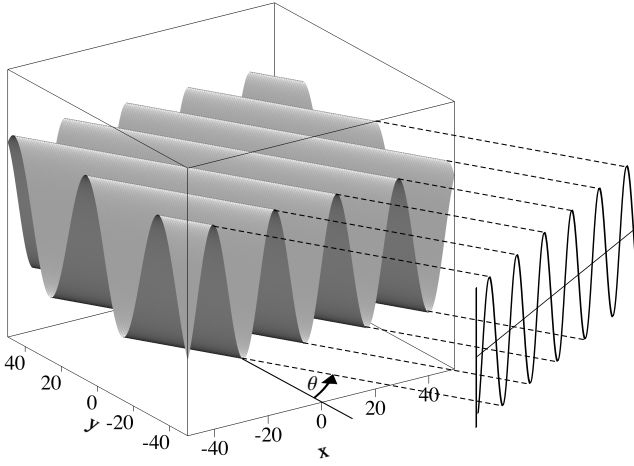


Fig. 13. A one-dimensional sinusoidal function shown backprojected at an angle of  $\theta = 30^\circ$ .

We shall revisit this important result (28) in due course. In the meantime, notice that in the case of a transmitted sinusoid  $P(k) = \delta(k - k_0)$ , the returned signal is, from (29),  $R'_x(k) = G(2k\hat{\mathbf{x}}')\delta(k - k_0) = G(2k_0\hat{\mathbf{x}}')$ ; that is, the Fourier transform of the ground patch is sampled at the location of the sinusoid in the  $2\mathbf{k}$ -plane, at a radius of  $2k_0$  and an angle of  $\theta$ .

### E. Backprojection and Impulse Reconstruction

We now examine the relationship between the monochromatic receiver signal (21) and the Fourier kernel in (26).

A *backprojection at an angle  $\theta$*  or  *$\theta$ -backprojection* is a two-dimensional signal which has been formed from a one-dimensional signal simply by positioning the one-dimensional signal in a two-dimensional space, oriented at angle  $\theta$  in the space, then smearing or extruding the one-dimensional signal at a right angle to  $\theta$  through the two-dimensional space. Think of the pattern made by a serrated knife dragged sideways across peanut butter. Fig. 13 demonstrates this principle with a sinusoid backprojected across the  $x$ - $y$  plane at  $\theta = 30^\circ$ . Mathematically, for some function  $f'(x')$ , simply define a two-dimensional function  $f'_b(x', y') = f'(x')$ , indicating no variation in the  $y'$  direction.

Applying the backprojection principle to the receiver signal for a centered impulsive scatterer under monochromatic illumination (21), we get

$$r'_b(x', y') = e^{jkx'}.$$

We have seen something like this before in converting  $kx'$  to the unrotated coordinate system in (4)–(6). With this conversion, we can express the backprojection of the receiver function from a centered scatterer in the  $x$ - $y$  system as

$$r_\theta(x, y) = e^{j\mathbf{k}\cdot\mathbf{x}}$$

where we have adopted a  $\theta$  subscript notation to explicitly indicate the direction of the backprojection in the unrotated  $x$ - $y$  system. This result is the same as (20) after converting (20)

to phasor form.<sup>9</sup> Thus the backprojection operation reconstructs the spatial field, restoring the spatial information that was lost when the receiver recorded only a slice of the wave field. An important observation here is that *a backprojection is a plane wave*. This is the same expression as the inverse Fourier kernel in (26). (Any concerns that we were using  $k$  or  $\mathbf{k}$  for two purposes should now be assuaged.) We might as well now write (26) as

$$\delta(\mathbf{x}) = \frac{1}{4\pi^2} \int r_\theta(x, y) d\mathbf{k}. \quad (30)$$

Arriving at this relationship is a central purpose of this paper. When viewing this result, remember that the context defining  $r'_b(x', y')$  here is that of a monochromatic wave and that  $\mathbf{k}$  carries both the necessary direction and frequency information. However, (30) indicates a summation of many monochromatic waves of different frequencies which is of course a polychromatic result. There are more adjustments to be made before we can consider this a result suitable for our radar problem.

Applying the same backprojection principle to the offset impulse receiver function under monochromatic illumination (19) results in

$$r_\theta(x, y) = e^{j\mathbf{k}\cdot(\mathbf{x}-2\mathbf{r}_s)} \quad (31)$$

which is the same as the kernel of the inverse Fourier transform (25) but with  $\mathbf{x}_0 = 2\mathbf{r}_s$ . Thus, a reconstruction formula identical to (30) also applies here but with  $r_\theta(x, y)$  defined for the offset scatterer as above and with the additional step that an image reconstructed from these ground patch measurements must be scaled by a factor of  $1/2$  to attain the correct size. This is easily done by relabeling the coordinate axes.

The reconstruction formula (30), being an integral, is linear and as such applies to any collection of impulsive scatterers  $g(\mathbf{x}) = \sum_n \gamma_n \delta(\mathbf{x} - \mathbf{x}_n)$  as a kind of discrete-scatterer case for any  $n$ . Since any ground patch can be written using the sifting property of the generalized Dirac function as  $g(\mathbf{x}) = \int g(\mathbf{y}) \delta(\mathbf{y} - \mathbf{x}) d\mathbf{y}$  as a continuous collection of impulses, we arrive at the important conclusion that any ground patch image can be reconstructed by backprojecting and summing all  $\theta$ -projections of all frequencies. We shall consider this in more detail in IV-G.

The preceding has shown two points. First,  $\theta$ -backprojection reconstructs the two-dimensional field that is due to a single transmission but which was lost due to sampling the field at only one point, and second, ground patch reflectivity functions can be reconstructed by summing these per-pulse reconstructed fields.

The form of (26) and (30) containing  $d\mathbf{k} = dk_x dk_y$  inspires a discretization in the manner of

$$d(\mathbf{x}) = \frac{1}{4\pi^2} \sum_n \sum_m e^{j(k_{x,m}x + k_{y,n}y)} \Delta k_x \Delta k_y \quad (32)$$

where  $k_{x,m} = m \Delta k_x$ ,  $k_{y,n} = n \Delta k_y$ ,  $m$  and  $n$  are integers, and where  $d(\mathbf{x})$  is taken as an approximate reconstruction of

<sup>9</sup>There are conceptually two  $x$ - $y$  coordinate systems: one defines the ground patch and the other is where the image is imagined to be reconstructed, either an abstract mathematical construct or as memory in a computer. We leave it to the reader to discern which is intended, as necessary.

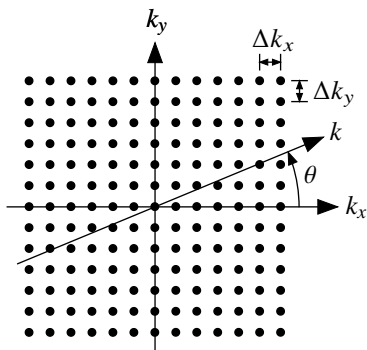


Fig. 14. Rectangular grid of two-dimensional impulses in the wavenumber domain, each represented by a dot. Each impulse represents a plane wave of wavenumber  $k$  propagating in direction  $\theta$ .

the impulse and should not be confused with the differential quantity  $dx$ . Using (27),  $d(\mathbf{x})$  has a Fourier transform

$$D(\mathbf{k}) = \frac{\Delta k_x \Delta k_y}{4\pi^2} \sum_m \sum_n \delta_2(k_x - k_{x,m}, k_y - k_{y,n}),$$

a two-dimensional series of impulses in the  $\mathbf{k}$  plane which at several points samples the unit function which is the Fourier transform of the centered impulse. A “textbook” discretization might assume  $\Delta k_x = \Delta k_y$ , leading to a bi-uniform sampling of the plane as depicted in Fig. 14. However, one could well specify  $\Delta k_x \neq \Delta k_y$  indicating a mapping from the bi-uniform case that indicates uniformity in each direction separately, or even a different style of discretization using different values for both  $\Delta k_x$  and  $\Delta k_y$ . In the case of two different choices of area, say  $(\Delta k_x \Delta k_y)_1$  and  $(\Delta k_x \Delta k_y)_2$  related by a differentiable mapping, the ratio of the areas reflects the Jacobian determinant of the mapping. Of course the usual rules of maximum allowable sampling interval must be observed to avoid spatial aliasing.

Fig. 15 shows the magnitude of a centered-scatterer back-projection reconstruction made from a rectangular grid of  $124 \times 124$  plane waves in the manner of Fig. 14 centered on the  $\mathbf{k}$  plane over a range in each direction of  $\pm 1.2\pi$ , making  $\Delta k_x = \Delta k_y \approx 0.0613$ ; the extent of the image is  $\pm 50 \times \pm 50$  spatial units plotted with  $256 \times 256$  pixels. The sampling intervals  $\Delta k_x$  and  $\Delta k_y$  have been chosen such that the first of the periodic aliases of the impulse appear at a distance of  $1/2 (\Delta k_x \text{ or } y/2\pi) = 51.25$ , just outside the plotted area; their near sidelobes can be seen appearing near the edges on the coordinate axes. In the preceding calculation the two in the denominator accounts for two-way propagation. Since any but a nearly central scatterer will cause at least one alias to appear within the plot, we see that the frequency sampling interval is too large by a factor of two in this illustrative example; halving both  $\Delta k_x$  and  $\Delta k_y$  would push the aliases out far enough that they would not appear on this particular example of a ground patch for any scatterer placement.

The preceding discussion has concentrated on image reconstruction based on a rectangular sampling grid in the wavenumber plane. While it is possible to make such a spotlight SAR in which the waveform generation is probably tractable, the design of the receiver becomes rather impractical,

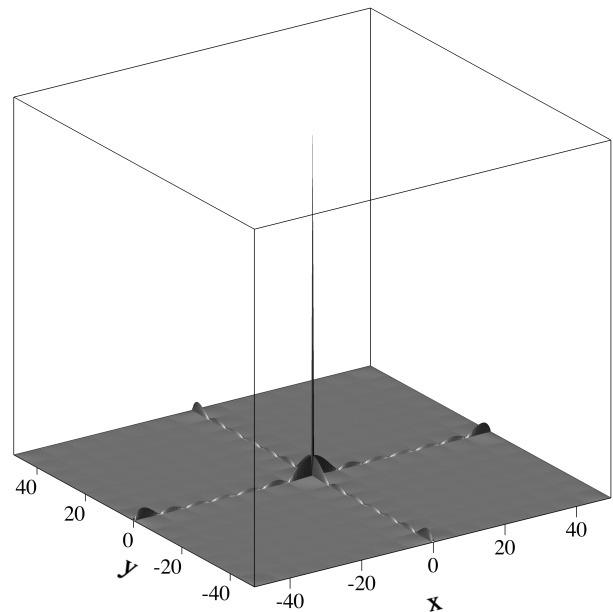


Fig. 15. Centered impulse reconstruction from plane waves represented as a bi-uniform grid of  $124 \times 124$  points in the Fourier plane ranging over  $k$  values of  $-2\pi 0.6$  to  $+2\pi 0.6$  in both dimensions.

a laboratory or turntable setting notwithstanding. Consider a radar platform steadily sweeping through an angle  $\theta$  while staring at a grid such as Fig. 14 but which in reality would have far more impulses to fill in. The waveform synthesizer would be very busy generating sine waves of various frequencies and at various times as  $\theta$  sweeps through the various known wavenumber domain impulse positions; the program would be deterministic but very challenging. However, the receiver would need to be matched to each reflection of the many transmitted sines, each at the appropriate time. In many instances the large number of narrow bandpass filters required to be generated simultaneously, along with the fact that the center frequencies of the filters in many cases would need to be very close, make this receiver design most likely impractical. However there is one advantage: the backprojections required can be implemented en masse at a great computational savings, without literal backprojections, by using an inverse Fast Fourier Transform algorithm operating on the whole batch of collected complex reflection amplitudes. The related process, called direct Fourier inversion, will be elaborated upon later but in a different context. This imaging concept was in fact described in a turntable setting in [39].

#### F. Spotlight SAR

The results of IV-E are interesting but not immediately applicable to the usual spotlight SAR scenario because that kind of radar naturally has data in the well-known polar format. A spotlight SAR operates typically by transmitting a signal, frequently a linearly frequency modulated (LFM) chirp [40], from each of many positions as the radar flies past the ground patch while the antenna dwells on the patch as in Fig. 1. Almost universally assumed is that the radar is stationary at a fixed  $\theta$  while each signal is transmitted and the reflections are

received, then advances to the next transmit-receive position, the so-called stop-and-go or stop-and-hop model [41, Ch. 21], [11]<sup>10</sup>. The general reflection model of Section III can handle any kind of signal including a chirp, but the monochromatic discussion of IV-B is potentially limiting. For present purposes, as we saw in making Fig. 15, we can somewhat work around this limitation by considering a series of monochromatic transmissions and combine the various backprojections by depending on linearity to get a polychromatic result. Working in this direction, consider that a series of monochromatic waves can be transmitted from each location  $\theta$  where the temporal frequency is an initial value and then increases by a constant amount for each additional frequency, that is,  $\{\omega_m = \omega_0 + m \Delta\omega\}_{m=0}^{M-1}$ , or similarly in terms of the wavenumber,  $\{k_m = k_0 + m \Delta k\}_{m=0}^{M-1}$ . If these are transmitted sequentially the waveform is known as a stepped sine [11], [43], [40]. They can also be transmitted simultaneously with similar results under certain conditions assuming that the receiver is matched accordingly [44], although there are many things to consider in choosing a waveform type. The stepped sign signal resembles a discrete sort of chirp signal.<sup>11</sup> The set  $\{k_m\}$  can also result as the bin centers of a possibly windowed inverse discrete Fourier transform performed on a demodulated chirp or other signal to get a time or space signal for backprojection after one-dimensional interpolation to image pixel locations from the discrete signal.

The other aspect of spotlight SAR that we need is angular diversity, so let us assume that each wideband signal or series of sine signals is sent and received from one of a set of stop-and-go angles  $\{\theta_n = n \Delta\theta\}_{n=0}^{N-1}$ . The descriptions of  $\{\omega_m\}$  or  $\{k_m\}$  and  $\{\theta_n\}$  both indicate a limitation on their range of values which, taken together, describe an angularly truncated annulus as in Fig. 16. This is the well-known polar formatted version of the transmitted signal [7], [1].

This takes us to the final adjustment needed in order for the sum-of-monochromatic-backprojections formula (30) to be fully appropriate for spotlight SAR impulse reconstruction. The polar formatted signal described above now may be conveniently cast in polar coordinates  $(k, \theta)_p$  due to the collection geometry of the SAR and its sweeping out a band of frequencies

<sup>10</sup>This model is mostly good in many applications but should always be considered carefully, especially in space-borne systems. In some cases a bistatic solution helps, with the transmitter and receiver in slightly different positions since the platform travels while the pulse is in flight. In others, a quasi-fan-beam geometry is helpful to understand and process the effects of a fast-moving platform. Both of these situations are considered to different degrees in [27] and bistatic systems generally are discussed widely. An application of relaxing the stop-and-go assumption in the case of frequency-modulated continuous wave SAR is [42].

<sup>11</sup>As a general principle, a receiver can record either the reflected signal or its Fourier transform, usually after being downconverted to baseband. The signal can be recorded directly or, for example, in the case of a monochromatic signal, its amplitude and phase can be detected; this is the Fourier transform. We shall not be too concerned here with the conceptual difference as the methods are essentially the same, differing by only a Fourier transform, but we do note that the time or spatial signal, not its Fourier transform, is needed for backprojection. Chirp receivers typically process the incoming signal so that the Fourier transform is received. One can see the similarity of detecting the magnitude and phase of a collection of sines by demodulating by multiplying each by a sine and cosine of the same frequency (in-phase and quadrature) then low pass filtering, and detecting the Fourier transform of a chirp by multiplying by I and Q versions of the chirp then low pass filtering.

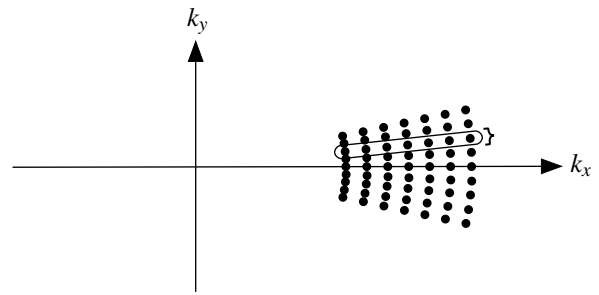


Fig. 16. Discrete points in the  $\mathbf{k}$  plane at the intersection of radial lines and concentric circles define the polar format sampling grid. Each dot represents an impulse and thus a plane wave.

from each angle. These  $\mathbf{k}$ -domain data are naturally crowded closer together nearer the origin as in Fig. 16. Recalling the earlier discussion of the Jacobian determinant and recalling from geometry that the determinant for rectangular-to-polar coordinates is  $|k|$ , (30) can be written

$$\begin{aligned} \delta(\mathbf{x}) &= \frac{1}{4\pi^2} \int_0^\pi \int_{-\infty}^\infty r_\theta(x, y) |k| dk d\theta \\ &= \frac{1}{4\pi^2} \int_0^\pi \int_{-\infty}^\infty e^{j\mathbf{k}\cdot\mathbf{x}} |k| dk d\theta \\ &= \frac{1}{4\pi^2} \int_0^\pi \int_{-\infty}^\infty e^{jkx'} |k| dk d\theta \end{aligned} \quad (33)$$

where as before, each  $r_\theta(x, y)$  should be remembered as a backprojection of a monochromatic receiver signal. This expression instructs simply that before adding a particular monochromatic plane wave  $e^{j\mathbf{k}\cdot\mathbf{x}}$  to the sum or integral, first weight it by its inherent wavenumber  $|k|$ . While for most radars operating over a narrow fractional bandwidth this correction is rather small in its effect [45], an overall scale factor notwithstanding, the operation is usually inexpensive and might as well be done.

Equation (33) might appear awkward, a kind of hybrid with the integrations performed in polar coordinates in the wavenumber domain but the result computed for the cartesian image domain. One might consider converting both to polar coordinates. Using the notation  $\mathbf{x} = (x, y) = (\rho, \phi)_p$  and  $\mathbf{k} = (k_x, k_y) = (k, \theta)_p$  to signify cartesian and polar coordinates in the  $\mathbf{x}$  and  $\mathbf{k}$  planes respectively, substituting into (33) results in

$$\delta_p(\rho, \phi)_p = \frac{1}{4\pi^2} \int_0^\pi \int_{-\infty}^\infty e^{jk\rho \cos(\phi-\theta)} |k| dk d\theta. \quad (34)$$

This form doesn't appear especially helpful at the moment but is useful in other contexts. But further examination of (33) reveals its utility as an algorithmic guide: select a  $k$  and a  $\theta$  from the polar format region of support, then compute  $e^{j\mathbf{k}\cdot\mathbf{x}}$  over a set of discrete points from the region of  $\mathbf{x}$  which corresponds to the image area that is being reconstructed. Repeat for different  $k$  and  $\theta$  until all of the available wavenumber-domain data are used. The entire  $\mathbf{k}$ -plane is indicated by the limits of the

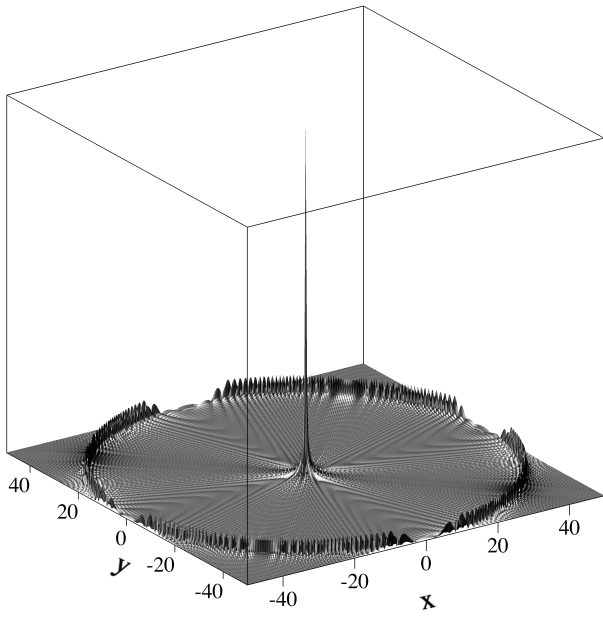


Fig. 17. Centered impulse reconstructed from summing plane waves sampled in the  $k$  plane and numbering 62 in the radial direction and 1440 in angle.

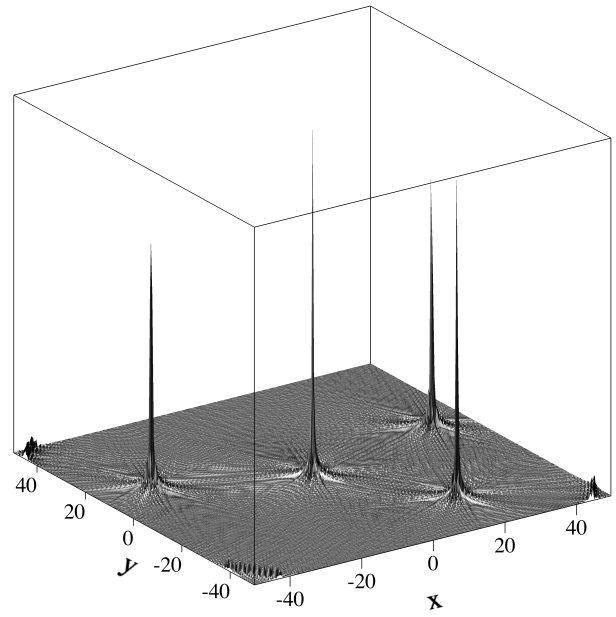


Fig. 19. Four impulses reconstructed from summing plane waves sampled in the  $k$  plane and numbering 124 in the radial direction and 1440 in angle.

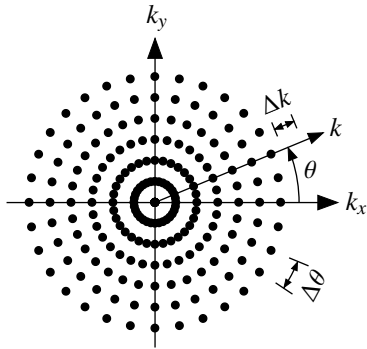


Fig. 18. Discretization parameters for a full-circle polar grid in the  $k$ -plane. Compare to Fig. 14.

integrals in (33) but of course the available data are from a finite support region.

Fig. 17 displays a magnitude backprojection reconstruction of a centered impulse according to an obvious discretization of (33). Let  $k_m = k_0 + m \Delta k$ ,  $\theta_n = \theta_0 + n \Delta \theta$ ,  $x_u = x_0 + u \Delta x$ , and  $y_v = y_0 + v \Delta y$  where  $m, n, u, v$  are all integers, so that  $\mathbf{k}_{m,n} = (k_m \cos \theta_n, k_m \sin \theta_n)$ ,  $|\mathbf{k}_{m,n}| = |k_m|$ , and  $\mathbf{x}_{u,v} = (x_u, y_v)$ . The locations of the points in  $\mathbf{x}_{u,v}$  are arbitrary but are usually chosen to coincide with the pixels in the reconstructed image which is scaled to represent the ground patch. Then the approximate reconstruction is

$$d(\mathbf{x}_{u,v}) = \frac{1}{4\pi^2} \sum_n \sum_m e^{j\mathbf{k}_{m,n} \cdot \mathbf{x}_{u,v}} |k_m| \Delta k \Delta \theta \quad (35)$$

which serves the same conceptual purpose as (32) except here the discretization is carried to the left-hand side, the reconstruction plane, simply for expository purposes. The visualization of this discretization plan is Fig. 18. Fig. 17 shows  $|d(\mathbf{x}_{u,v})|$  constructed from plane waves represented by a densely-sampled  $k$  plane with  $k$  varying from 0 to  $1.2\pi$

radians/m (0 to 0.6 cycles/m) in 62 samples and  $\theta$  varying around the entire circle in 1440 samples which is enough to prevent angular aliasing in this example. Here, the radial sampling rate in the  $k$  plane is the same as the sampling rate in either direction in Fig. 15. Rather than fully-realized aliased copies appearing periodically, in this case the aliased energy appears as a ring of radius 51.25 surrounding the impulse. Other alias rings appear at multiples of 51.25 and are not shown in the figure. Once again, this under-sampling is done intentionally for illustrative purposes. This particular form of aliasing is analyzed in terms of Hankel transforms and Bessel functions in [44].

Fig. 19 shows a reconstruction of four impulses located in the  $x$  plane at  $(0, 0)$ ,  $(40, 10)$ ,  $(-35, 15)$ , and  $(20, -30)$ , made according to (31) and with a discretization similar to (35). This is an example in showing the utility of the off-center field and receiver functions such as (7) and (10) and indicates how a general ground patch can be imaged. Relative to Fig. 17, the radial sampling interval in the  $k$  plane was roughly halved by increasing the number of samples to 124 over the same range of 0 to  $1.2\pi$ ; this is enough to prevent aliased energy from appearing within a circle with a radius of about 51.25 as discussed in connection with Fig. 17, even for reflectors or impulses placed at the edge of that circle. Aliasing artifacts can be seen outside this radius in three of four corners of the figure. If the ground patch image is considered to be the entire square then the radial sampling interval in the  $k$  plane must be further diminished by a factor of  $1/\sqrt{2}$ , the distance in the  $x$  plane from the center to the nearest edge divided by the distance from the center to a corner.

As a final example consider Fig. 20 which uses the same scatterer positions as Fig. 19 but restricts the bandwidth of the  $k$  plane support to something somewhat more radar-like while keeping the same  $k$  plane sampling density. The angular

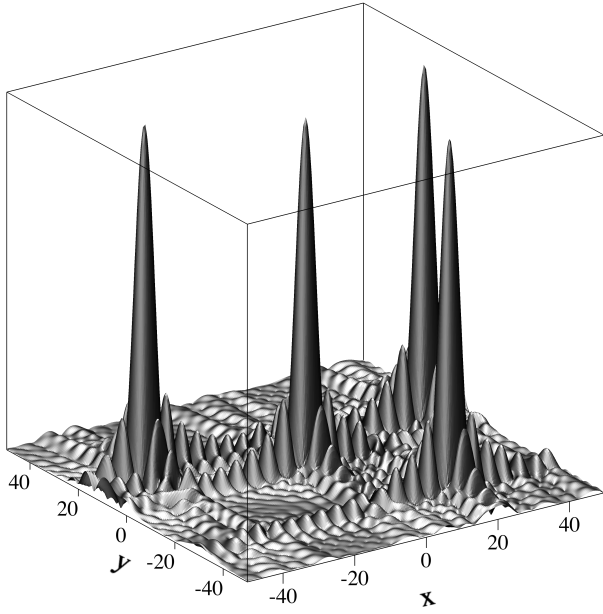


Fig. 20. Four impulses reconstructed from summing plane waves sampled from a restricted region in the  $\mathbf{k}$  plane and numbering 24 in the radial direction and 25 in angle.

variation in  $\mathbf{k}$  is limited to  $\pm 6$  degrees centered on the  $k_x$  axis while the radial variation is limited to  $[4.8625, 6]$ , a 21% bandwidth. This bandwidth limitation is in the manner of Fig. 16 but with different limits than shown there. For convenience here, the radial bandwidth limitation has been affected by a notional  $P(k)$  from IV-D that perfectly limits the radial frequency range. Both of these limited ranges are perhaps double that of what might normally be considered a wideband radar. Since the  $\mathbf{k}$  plane support is roughly square, the reconstructed impulses show a significant  $\text{sinc}(\cdot)\text{sinc}(\cdot)$  character; the radial and angular limitations were chosen to present a roughly square support of the main lobes. A two-dimensional window can be applied to the frequency domain data before the image is calculated in order to reduce the sidelobe level but with a widening of the main lobes. It should be noted that the choice of image size to be constrained to  $\pm 50$  in each dimension is arbitrary and an actual ground patch image would be larger so that the reconstructed impulses shown here would occupy a smaller portion of the total image.

### G. Backprojection Generally

We have informally developed a method to reconstruct a ground patch consisting of a single impulse, claimed that ground patches of multiple impulses can be reconstructed using the same method, and claimed further that any ground patch, even a continuous one, can also be so reconstructed. We have shown numerically-derived graphical reconstructions using discretized versions of the method. One purpose of this approach has been to show that a backprojection is a plane wave and to relate that idea to Fourier synthesis. We now formalize this method a little.

Beginning with the two-dimensional Fourier transform of the ground patch reflectivity function then converting to polar

coordinates in the wavenumber plane,

$$\begin{aligned} g(\mathbf{x}) &= \frac{1}{4\pi^2} \int G(\mathbf{k}) e^{j\mathbf{k}\cdot\mathbf{x}} d\mathbf{k} \\ &= \frac{1}{4\pi^2} \int_0^\pi \int_{-\infty}^\infty G(k \cos \theta, k \sin \theta) \cdot \\ &\quad e^{jk(x \cos \theta + y \sin \theta)} |k| dk d\theta \quad (36) \\ &= \frac{1}{4\pi^2} \int_0^\pi \int_{-\infty}^\infty G(k\hat{\mathbf{x}}') e^{jk\mathbf{x}\cdot\hat{\mathbf{x}}'} |k| dk d\theta \\ &= \frac{1}{4\pi^2} \int_0^\pi \int_{-\infty}^\infty G'(k) e^{jkx'} |k| dk d\theta \end{aligned}$$

the last line following from the Projection Slice Theorem (28) and that  $\mathbf{x} \cdot \hat{\mathbf{x}}' = x'$  from (4). Let  $\mathcal{F}^{-1}\{|k|\} = q(x')$ . Then the inner integral is

$$\mathcal{F}^{-1}\{G'(k)|k|\} = g'(x') * q(x') \equiv \bar{g}'(x'). \quad (37)$$

Finally,

$$g(\mathbf{x}) = \frac{1}{2\pi} \int_0^\pi \bar{g}'(x') d\theta \quad (38)$$

which is a general form of the reconstruction of projections of  $g(\mathbf{x})$ . Notice that  $q(x')$  is not a function of  $\theta$ , unlike  $g'(x')$ , and must be computed only once. Also,  $|k|$  is a generalized function [36] and must be approximated in applications. One method is to place a lowpass window over  $|k|$  which also tends to alleviate the emphasis of high frequency noise.

Equation (38) is known as Radon's inversion formula. It is interpreted as filtering—convolving—each projection  $g(x')$  with a filter with frequency response  $|k|$  and then  $\theta$ -backprojecting each filtered projection and summing all  $\theta$ -backprojections. This is the source of the commonly-used name, *convolution-backprojection*. The convolution indicated by (37), in a discretized version, might be more efficiently implemented using the Fast Fourier Transform in the  $k$ -domain. Regardless of how the filtering is done, the method is considered a spatial-domain algorithm, or sometimes, rather oddly, it is called a time-domain algorithm.

The above discussion is again devoid of any radar aspects but is appropriate for computerized tomography (CT) applications. To cure this, notice that the only information available to the radar is  $r'_x(x') = g'(x') * p(2x')$ , (17). All we can do, apparently, is to backproject  $r'_x(x')$  adapted for polar coordinates—polar format:

$$\begin{aligned} \bar{r}'_x(x') &\equiv \bar{g}'(x') * p(2x') \\ &= g'(x') * p(2x') * q(x') \end{aligned}$$

and

$$\bar{R}'_x(k) = G'(2k) P(k) |k|.$$

Here, the convolution with  $p(2x')$  enters as being caused by the physics of the propagating radar signal and convolution with  $q(x')$  follows from the fact that the radar is designed to sample the  $\mathbf{k}$ -domain on a polar grid. This modified receiver signal will not reconstruct  $g(\mathbf{k})$  exactly because of the distorting influence of  $p(2x')$  and  $P(k)$ , so define a new approximate reconstruction

$$\tilde{g}(\mathbf{x}) = \frac{1}{2\pi} \int_{\Theta} \bar{r}'_x(x') d\theta. \quad (39)$$

$P(k)$  is normally made from a lowpass baseband signal modulating a sinusoidal carrier and thus it effectively filters  $G'(2k)|k|$  into a bandpass signal centered on the carrier frequency. The range of integration over  $\theta$  has been indicated so far as  $[0, \pi)$  because the radial integration limits are  $[-\infty, \infty)$  and also because of the symmetry  $g'(\theta, x') = g'(\theta + \pi, -x')$ . Obviously, any contiguous span of distance  $\pi$  would work mathematically, and for the radar geometry presented earlier, a range of  $[-\pi/2, \pi/2)$  makes more sense. Above in (39), the notation  $\Theta$  has been used to indicate any support subset as necessarily defined by the operation of the radar but which support is normally a contiguous subset ranging from some  $\theta_{min}$  to some other  $\theta_{max}$ . And actually, to be respectful of the radar scenario and recognizing that only a discrete set of possibly sparse projections will be measured, it is possible to collect the discrete projections from  $[0, 2\pi)$  without any duplicates being measured; a discretized version of (39) would allow for this possibility and establish a finite  $\Delta\theta$  for each projection, with care taken to account for any situation where projections are measured from both  $\theta$  and  $\theta + \pi$ . Together, the combined actions of  $P(k)$  and  $\Theta$  act to cause spotlight SAR to be considered as a kind of bandpass version of CT a la Fig. 16 with exemplar reconstruction Fig. 20 but with the additional difference that SAR is coherent—it measures phase and thus collects complex-valued data—while CT is incoherent, as noted in [1].

#### H. Computational Considerations

We have so far developed an interpretation of spotlight SAR imaging as an additive combination of weighted monochromatic plane waves, clarifying the intimate connection between wave theory and the signal processing concepts of the Fourier and Radon transforms. This notion is the central purpose of this paper and should be kept firmly in mind. The images of Fig. 15, Fig. 17, Fig. 19, and Fig. 20 were constructed literally in this way. However, this is a highly inefficient method, requiring far more calculations than is necessary. There have been many works written on the details of all aspects of this topic, some of which are listed in Section I, but here we shall touch only lightly on a few conceptual matters of importance. In so doing we shall highlight the differences and the essential sameness of two popular classes of SAR image reconstruction methods, convolution-backprojection and direct Fourier inversion also known as the polar format algorithm (PFA)<sup>12</sup>.

We have concentrated on the backprojection of monochromatic waves as a tool to easily tie together simple wave mechanics with signal processing, but by now it is obvious that there is a more efficient way, and we have in fact already seen it. Consider (36), re-written here as

$$g(\mathbf{x}) = \frac{1}{4\pi^2} \int_0^\pi \underbrace{\int_{-\infty}^{\infty} G(\mathbf{k}) e^{j\mathbf{k}\cdot\mathbf{x}} |k| dk}_{\Delta k} d\theta. \quad (40)$$

Discretizing the above in the manner of (35) helps to clarify the processing. Allowing for possibly unequal  $\Delta k$ s and

$\Delta\theta$ s—especially useful for the latter in cases where the moving platform or pulse transmission program or engagement scenario does not allow for equal angular increments—allows the approximation of  $g(\mathbf{x})$

$$\hat{g}(\mathbf{x}_{u,v}) = \frac{1}{4\pi^2} \sum_n \underbrace{\sum_m G(\mathbf{k}_{m,n}) e^{j\mathbf{k}_{m,n}\cdot\mathbf{x}_{u,v}} |k_m| \Delta k_m \Delta\theta_n}_m \quad (41)$$

which approximation might also include band limiting in wavenumber or view angle or both. The backprojection operation is very expensive and should be done as rarely as possible. Backprojecting each of the sinusoidal components of (40) or (41) thus is not a good idea. Instead, consider the inner integral in (40) or the inner summation over  $m$  in (41) as indicated by the brace in either the continuous or the discrete case. Backprojection is linear so a much more efficient method is to sum these components before backprojecting the sum only once. The backprojected function is no longer a monochromatic wave but a polychromatic wave as alluded to earlier. This summation is a one-dimensional Fourier synthesis operation. Fig. 16 is apropos here as a mental picture, with the circled group of  $\mathbf{k}$ -plane impulses representing a particular summation over  $m$  for a fixed angular index  $n$ . This summation reduces the operation count from  $O(N^4)$  to  $O(N^3)$ . We shall not explore this concept deeply, but roughly, without summing, the number of operations is number of  $u$  pixels  $\times$  number of  $v$  pixels  $\times$  number of  $\theta$  angles  $\times$  number of  $k$  frequency points. The summation collapses the final component of that count. Fast algorithms for backprojection have been reported, e.g. [46], reducing the operation count to  $O(N^2 \log N)$ , but at least some of these algorithms require approximations, potentially causing compromises in image quality—[46] claims minimal degradation. However, the desire to reduce the operation count is sometimes found in practice to be compelling.

The reconstructions in the image figures herein took advantage of the fact that the backprojected functions could be computed exactly at every point  $(u, v)$ , those functions being sinusoids. In practice this luxury is not available because the filtered projections are known only on a set of discrete points oriented at angle  $\theta$  and are derived from the unknown ground patch and thus must be treated to a one-dimensional interpolation to each image pixel during backprojection. This step unavoidably induces errors and has been itself a focus of several studies to find acceptable interpolators. This one-dimensional interpolation adds to the computational burden.

Switching attention now to direct Fourier inversion, consider once again Fig. 16 but also the rectangular format rendering of Fig. 14. Again, each dot of these figures represents a weighted impulse in the  $\mathbf{k}$ -plane, a complex-valued sample of  $G(\mathbf{k})$  representing a magnitude and phase. As described before, each dot can be converted to a sinusoid and backprojected, with the rectangular grid suffering a disadvantage because there is no opportunity to group impulses along the radial variable  $k$  and thus no opportunity to exploit the Projection Slice Theorem. However, in either the rectangular case or the polar case with  $|k|$  weighting, such backprojections of individual sinusoids, summed in the image plane  $\mathbf{x}$ , represent a Fourier synthesis, an inverse (discrete) Fourier transform. But in the rectangular

<sup>12</sup>“Polar format algorithm” seems to imply a single algorithm where in fact there are many variations. “Direct Fourier inversion” seems less presumptuous but as we shall see, it too is perhaps not so unambiguously descriptive.

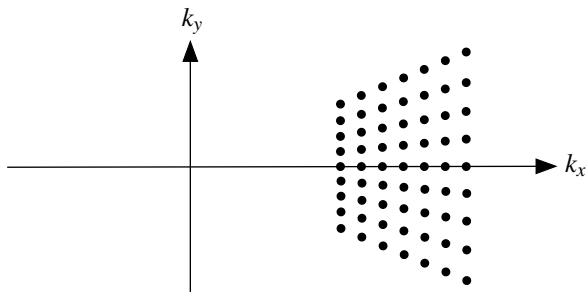


Fig. 21. Discretization points in the  $k$ -plane for a keystone format achieved by adjusting the waveform slightly from pulse to pulse, thus requiring only one-dimensional interpolation to adapt it for FFT processing.

format case there is the opportunity to employ the inverse Fast Fourier Transform since the samples lie on a grid which can immediately be accommodated into the FFT structure. This has been an extremely important advantage historically because of the efficiency of the FFT and reduces the overall operation count to  $O(N^2 \log N)$ .

The polar format therefore stands at a disadvantage but polar-formatted data are the natural format for spotlight SAR. To compensate, polar-formatted data can be interpolated to a rectangular grid; once that is done, the FFT can be used and its efficiency gain enjoyed. This does not come for free since the two-dimensional interpolation is itself an expensive operation. Still, practice has shown that the combined operation of two-dimensional interpolation followed by inverse two-dimensional inverse FFT, direct Fourier inversion, is still faster on most computing architectures than convolution-backprojection, purpose-built, workstation clusters, or parallel-processor computers notwithstanding, but this is a complicated subject and results vary [47], [48] and should be considered in light of the aforementioned fast backprojection algorithms.

There is a way to ease the burden of the two-dimensional interpolation by placing a slight burden on the transmitter. Each pulse can be modified from the preceding pulse by subtly compressing or expanding it in time [49], [44] causing an inverse amount of expansion or compression in its spectrum. This can be programmed into the waveform synthesizer of the transmitter. If this is done on a particular schedule, a keystone format can be achieved as shown in Fig. 21. This then requires only a one-dimensional interpolation, along lines parallel to the  $k_y$ -axis, before applying the inverse FFT. A similar effect can be achieved by slightly altering the analog-to-digital sampling rate [49].

### I. Convolution-Backprojection versus direct Fourier inversion

We see that convolution-backprojection and direct Fourier inversion both operate on the same principle, that of summing weighted plane waves—Fourier synthesis as represented by (22). As such, they are fundamentally the same, differing mainly in implementation details. Convolution-backprojection can work on any distribution of plane-wave samples in the  $k$ -plane whatsoever as long as proper weight is given to each sample's share of surrounding area, the Jacobian or some similar measure if there is no appropriate mapping to a uniform sampling grid.

It works for example on Fig. 14, Fig. 16, Fig. 21, or even some haphazard or unorganized distribution of impulses. It just happens that if the data are polar-formatted, some computational savings accrue. Indeed, we see that convolution-backprojection is nothing but a “slow” inverse Fourier transform.

If the  $k$ -plane samples happen to lie on a rectangular grid with not necessarily equal  $\Delta k_x$  and  $\Delta k_y$ , then the inverse FFT can be applied with typically, but not always, great computational savings. If the data do not lie on such a grid, it is necessary, if a well-focused image is desired, to resample the data to such a rectangular grid. Some authors state that this resampling is required in order to obtain the image but it is required only if the efficiency of the FFT is desired.

Convolution-backprojection works on polar data by computing a one-dimensional inverse (discrete) Fourier transform, DFT, after weighting by the Jacobian  $|k|$ , then doing a one-dimensional interpolation in the spatial domain  $x$ -plane as the backprojection is performed. Direct Fourier inversion does a kind of reversal of those steps, interpolating in the  $k$ -plane before doing an inverse two-dimensional DFT probably using an FFT.

Some researchers have reported better images using one method over the other as though they are fundamentally different processes, backprojection usually being considered better. Any differences between a convolution-backprojection reconstruction and a direct Fourier inversion reconstruction are due to numerical choices such as interpolation, windowing, assignment of Jacobian values in non-trivial distributions, and use or non-use of portions of the polar data that do not get incorporated in the two-dimensional interpolation of a direct Fourier inversion. Comparison studies are reported in [47], [50], [48], [51], and [52]. Some ruminations on this topic are in [19].

The convolution-backprojection computation can proceed apace as each pulse reflection is received. Direct Fourier inversion must wait until the last reflection to be processed is received and then process all of the data at once, as a batch, regardless of whether a FFT is used. This means that there is the potential for convolution-backprojection to finish sooner and the potential that maximum computational throughput can be less than direct Fourier inversion. Details vary by application, of course.

Related to the above, the convolution-backprojection image can be viewed as it develops, at first in low resolution and then with increasing resolution as more data are received and backprojected.

The convolution-backprojection does not have to have pixels on a rectangular grid (for example, (34) indicates how a polar image can be developed) or on any particular pixel arrangement at all; the points selected in the  $x$ -plane can be selected at will, although the normal method is indeed a regular pixel grid. This does lead to an advantage, however. If only a portion of the image contains objects of interest, the remaining part does not need to be developed, or it can be developed with lower resolution. Direct Fourier inversion is limited to the strictures of the FFT—regular rectangular sampling in both domains.

While we have concentrated on the plane wave approximation, convolution backprojection can be directly, easily, and

naturally modified to account for any amount of wavefront curvature in both monostatic and bistatic radars [28], [29], [27], [30], [31], [32], [52]. This is accomplished without the separate focusing steps required of typical direct Fourier inversion methods which present a substantial additional processing burden and often obtain only a partial correction. In bistatic geometries, wavefront curvature manifests as elliptical contours of equal time-of-flight and thus elliptical line integrals, for a flat earth, requiring elliptical backprojections. A comment in [53] reads like this: “Among its classical advantages, [backprojection] focussing accuracy does not depend on the carrier wavelength, the desired resolution, the scene size or the imaging configuration. Time-domain image formation [sic] offers a further advantage particularly useful in the case of bistatic systems: precise accommodation of irregular sampling schemes. ...another strong advantage of [backprojection] with respect to Fourier-domain [sic] techniques is the possibility of precise range- and azimuth-variant antenna filtering and weighting.” There is also this comment in [32]: “In order to evaluate frequency-domain processors that all have to use some kind of approximations, a flexible bistatic time-domain processor was implemented. This processor can be used as a reference processor because it is based on the matched-filter principle and models the SAR geometry exactly [29, local reference]. Provided that the platform tracks are known to the order of fractions of the wavelength, such a processor can be applied universally to any bistatic configuration, even if the platforms move on curved orbits.” Backprojection methods have been adapted for arbitrary monostatic and bistatic flight paths including full-circle, plus propagation attenuation correction, nonflat topography, and antenna shading [27], [29], [30], [54], [55], [52]. There is some reason to believe that convolution-backprojection could be adapted for near field (non-spherical, non-planar) applications as well, as long as the equal time-of-flight paths are known. Other advantages of backprojection methods include the possibility to account for quasi-fan beam geometries, a potentially valuable feature where high-speed platform motion or long pulses can cause intra-pulse distortion [27]. Convolution-backprojection methods can be implemented on parallel computing architectures [47], [56], the method being somewhat of a natural fit.

As the bandwidth of the transmitted signal increases and as the range of look angles  $\theta$  increases, the interpolation required for direct Fourier inversion becomes more complicated as the samples deviate more from nearby rectangular grid points and the increasing included angle of the arc fits more awkwardly into a nice FFT rectangle, whereas reconstruction by backprojection proceeds without further complications; indeed, [27] showed many simulation examples of full-circle spotlight SAR using an impulsive signal.

Direct Fourier inversion tends to have a reduced computational advantage as the image size is reduced. It has been said [46] that the advantage tends to be lost for image sizes less than  $1,000 \times 1,000$  but this is no doubt a rough guide depending on many factors.

The above claims for advantages of convolution-backprojection are not meant to imply that direct Fourier inversion can not be adapted to advantage. For example,

CT scanners can sort discrete line integrals from separate fan projections into groups of equal  $\theta$  for processing as parallel-beam CT. Direct Fourier inversion has also been modified to other spotlight SAR scenarios including correction for monostatic wavefront curvature using range migration [57], [58], [14].

As a mini-summary of the two methods, consider that convolution-backprojection can readily handle arbitrary distributions of wavenumber domain data and is especially good with polar format data, requires a Jacobian weighting or at least an appropriate  $\Delta k \Delta \theta$  for each data point, performs the required summation in the spatial domain, and can be slow unless special fast algorithms or hardware are employed. Direct Fourier inversion requires data to be on a rectangular grid and therefore requires two-dimensional interpolation from arbitrary or polar data thus starting the inversion process from a different set of points, performs the summation in the wavenumber domain, requires no Jacobian correction, and enjoys the efficiency of the FFT.

## V. SUMMARY AND COMMENTS

An intuitive explanation and interpretation of the use of backprojection in forming spotlight synthetic aperture radar images has been presented. A radar signal propagation model incorporating the spotlight geometry under the plane wave assumption was developed from first principles, the wave equation and some simple solutions in the radar context. This model does not specify the form of the transmitted signal and so is suitable for any signal. The propagation model was solved to describe both the time-domain and space-domain signal that arrives back at the radar. The model was applied first to a single point scatterer and then to specialized collections of point scatterers arranged along the rotated coordinate axes, finally being generalized to a continuous collection of scatterers, the ground patch reflectivity. This resulted in the important result that the reflected signal is the convolution of the transmitted signal with a projection of the ground patch reflectivity. Next, a specific signal was selected, the monochromatic plane wave. The intimate connection between monochromatic plane waves and the Fourier transform was demonstrated and the concept of backprojection was introduced with the satisfying result that the operation restores the spatial information, the full plane wave, that was lost by sampling the reflected wave at only one point, the receiving antenna. It was shown that highly focused impulses could be reconstructed by backprojecting a variety of monochromatic received signals covering a wide range in the two-dimensional frequency domain in both rectangular and polar formatted data, and how less well-resolved images could be constructed from a limited range of spatial frequency information. The all-important Projection Slice Theorem was derived, connecting projections and Fourier transforms even more closely. Due to the general signal model, it was shown how to correct the undesirable effects of a general pulse shape including but not limited to the popular linear frequency modulation (LFM). After this lengthy introduction, the full backprojection method for a general pulse and general ground patch was introduced, by now allowing a good comprehension

of how and why backprojection works. This led naturally into a discussion of computational considerations and a comparison of convolution-backprojection and direct Fourier inversion, the polar format algorithm. These methods were shown to be the same in their theoretical underpinning but differing in implementation details.

Chirp signals [40] wherein the phase of a sinusoid is made to change quadratically with time so that the frequency changes linearly with time, usually with an offset frequency due to a RF carrier, are commonly used. The theory of LFM and demodulation in the context of spotlight SAR is thoroughly covered in [1]. These signals are compatible with the presentation herein but due to their special nature are especially attractive for this application. Typically the demodulation results in a signal which can be cast directly in polar format form in the  $k$ -domain and thus requires an inverse Fourier transform before being suitable for backprojection.

By default, so far, it has been assumed that the signal which is to be backprojected is the bandpass signal which is carried on a radio frequency (RF) carrier. This would be an arduous task not the least because of the difficulty of sampling the RF signal directly. Radar receivers normally convert the bandpass signals centered on the RF carrier frequency to baseband via time-domain processing before digitizing and processing for myriad reasons. While the per-pulse demodulation is done by the receiver, it is convenient to envision that, in the case of direct Fourier inversion, a two-dimensional demodulation is carried out as follows. The data are conceptually arrayed in the  $k$ -plane as in Fig. 16. The correct demodulation to baseband takes place by simply translating the entire constellation intact towards the origin so that it is more or less centered there. This is really a conceptual translation and nothing needs to be done as long as the data in computer memory are interpreted as though they are arrayed near the origin. The translation affects only the phase of the image, not the magnitude, so the direct Fourier inversion by FFT yields the same magnitude image but with a dramatically increased efficiency since a raft of zero-value samples need not be processed [1]. This bulk demodulation is distinctly different from a process of demodulating each return signal separately in one dimension and sliding it towards the origin of the  $k$ -plane which will give the wrong result, a star-like or wedge-like constellation centered on the origin, not the desired shape. In the case of backprojection, the receiver demodulation implies the same pulse-by-pulse translation along the respective  $k'_x$  axes towards the origin. In order to maintain the advantage of the projection-slice theorem, a spatial remodulation outward along the  $k'_x$  axes is usually implemented [1], [50], compensating for the temporal modulation which was removed in the receiver. Remember that spatial frequencies are  $c/2$  times smaller than temporal frequencies.

At the outset we stated that one of the assumptions is a two-dimensional geometry, in effect, a flat earth. Most synthetic aperture radars operate with this assumption to good effect. The mapping from the slant plane to the ground plane is straightforward, mostly just a scaling of the range dimension. However, in the presence of significant deviations from flatness, image distortions called *layover* will appear

which can be challenging for human image interpreters to understand. Examples are hills and mountains, valleys and canyons, trees, open mine pits, and tall buildings. Other distortions can appear if the radar moves out of the slant plane. There is a signal processing solution to this situation but it comes at a significant cost: expand the geometry to three dimensions [15]. Under the plane wave assumption, the equal time-of-flight loci which are the basis for the mathematical concept of projections are then planes rather than lines as studied earlier.

The idea of using backprojection in spotlight SAR is nearly 40 years old but the polar format algorithm and its variants still dominate. In light of the fact of much faster hardware, fast algorithms, and the adaptivity of backprojection to arbitrary amounts of wavefront curvature and arbitrary flight paths in monostatic and multistatic modes, a remark in a rather recent work [13] could be interpreted to mean that it might be time to take another look at backprojection: "The [polar format] algorithm was born in an era when computing resources were scarce, and the limitations of PFA were seen as a fair trade for its efficiency. ...wide-beam imaging violates the tomographic [linear projections leading to polar format algorithm] assumption. ...we must be careful to approach new problems afresh, asking which processing chain is best suited to the given constraints."

Many engineers have at one time or another found themselves measuring the transfer function of an electronic circuit, a mechanical structure, or a loudspeaker. To find the response at a particular frequency, a sine wave is injected and the response, real and imaginary or magnitude and phase, is measured at some other point. If the response is desired at multiple frequencies, the sine frequency is varied and the results plotted. Some applications use an exponential chirp with a matched filter [59]. Sometimes these frequency data are inverse Fourier transformed to get an impulse response estimate. Spotlight SAR is the same, but in two dimensions, with the ground patch as the system being measured and the image as the estimated impulse response. In both cases, the measurement includes the measuring equipment which is hoped to have minimal effect or is able to be deconvolved away, and in both cases the inverse Fourier transform tends towards the impulse response as the measurement bandwidth increases.

The presentation in this paper has been focused on the particular aspect of how backprojection arises in spotlight SAR image reconstruction and to do that many aspects of spotlight SAR and radar generally have been left out. These aspects can be incorporated with the reader's previous or future understanding.

## REFERENCES

- [1] D. C. Munson, J. D. O'Brien, and W. K. Jenkins, "A tomographic formulation of spotlight-mode synthetic aperture radar," *Proceedings of the IEEE*, vol. 71, no. 8, pp. 917–925, Aug 1983.
- [2] W. M. Brown and L. J. Porcello, "An introduction to synthetic-aperture radar," *IEEE Spectrum*, pp. 52–62, September 1969.
- [3] J. C. Curlander and R. N. McDonough, *Synthetic Aperture Radar: Systems & Signal Processing*, ser. Wiley Series in Remote Sensing. New York: John Wiley & Sons, Inc., 1991.
- [4] T. P. Ager, "An introduction to synthetic aperture radar imaging," *Oceanography*, vol. 26, no. 2, pp. 20–33, 2013.

- [5] A. Moreira, P. Prats-Iraola, M. Younis, G. Krieger, I. Hajnsek, and K. P. Papathanassiou, "A tutorial on synthetic aperture radar," *IEEE Geoscience and Remote Sensing Magazine*, vol. 1, no. 1, pp. 6–43, March 2013.
- [6] I. H. Woodhouse, *Introduction to Microwave Sensing*. Boca Raton, Florida: CRC, Taylor & Francis Group, 2006.
- [7] J. L. Walker, "Range-doppler imaging of rotating objects," *IEEE Transactions on Aerospace and Electronic Systems*, vol. AES-16, no. 1, pp. 23–52, Jan 1980.
- [8] D. R. Wehner, *High Resolution Radar*. Norwood, Massachusetts: Artech House, 1987.
- [9] R. Yang, H. Li, S. Li, P. Zhang, L. Tan, X. Gao, and X. Kang, *High-Resolution Microwave Imaging*. Beijing and Singapore: National Defense Industry Press and Springer Nature Singapore Pte Ltd., 2018. [Online]. Available: <https://doi.org/10.1007/978-981-10-7138-6>
- [10] B.-C. Wang, *Digital Signal Processing Techniques and Applications in Radar Image Processing*, ser. Information and Communications Technology Series. Hoboken, New Jersey: John Wiley & Sons, 2008.
- [11] M. A. Richards, *Fundamentals of Radar Signal Processing*, 2nd ed. New York: McGraw-Hill Education, 2014.
- [12] K.-S. Chen, *Principles of Synthetic Aperture Radar Imaging: A System Simulation Approach*. Boca Raton, Florida: CRC Press, Taylor & Francis Group, 2016.
- [13] W. L. Melvin and J. A. Scheer, Eds., *Principles of Modern Radar: Advanced Techniques*. Edison, New Jersey: Scitech Publishing, an imprint of Institution of Engineering & Technology, 2013, vol. II.
- [14] W. G. Carrara, R. M. Majewski, and R. S. Goodman, *Spotlight Synthetic Aperture Radar: Signal Processing Algorithms*, ser. Artech House Remote Sensing Library. Boston: Artech House, 1995.
- [15] C. V. Jakowatz, Jr., D. E. Wahl, P. H. Eichel, D. C. Ghiglia, and P. A. Thompson, *Spotlight-Mode Synthetic Aperture Radar: A Signal Processing Approach*. Springer Science & Business Media, Inc., 1996.
- [16] J. P. Fitch, *Synthetic Aperture Radar*. New York: Springer-Verlag, 1988.
- [17] M. Soumekh, *Synthetic Aperture Radar Signal Processing with MATLAB Algorithms*. New York: John Wiley & Sons, Inc., 1999.
- [18] R. E. Blahut, *Theory of Remote Image Formation*. Cambridge, United Kingdom: Cambridge University Press, 2004.
- [19] C. F. Barnes, *Synthetic Aperture Radar: Wave Theory Foundations*. Powder Springs, Georgia: C. F. Barnes, 2014.
- [20] S. R. Deans, *The Radon Transform and Some of Its Applications*. New York: John Wiley & Sons, 1983.
- [21] G. T. Herman, *Image Reconstruction from Projections: The Fundamentals of Computerized Tomography*. New York: Academic Press, 1980.
- [22] A. C. Kak and M. Slaney, *Principles of Computerized Tomographic Imaging*. New York: IEEE Press, 1987.
- [23] D. E. Dudgeon and R. M. Mersereau, *Multidimensional Digital Signal Processing*. Englewood Cliffs, New Jersey: Prentice-Hall, 1984.
- [24] S. Haykin, J. H. Justice, N. L. Owsley, J. L. Yen, and A. C. Kak, *Array Signal Processing*, S. Haykin, Ed. Englewood Cliffs, New Jersey: Prentice-Hall, Inc., 1985.
- [25] O. Frey, "A collection of literature on synthetic aperture radar (SAR)." [Online]. Available: <http://www.ifu-sar.ethz.ch/otfrey/SARbibliography/index.html>
- [26] W. L. Stutzman and G. A. Thiele, *Antenna Theory and Design*. John Wiley & Sons, 1981.
- [27] J. L. Bauck, "Tomographic processing of synthetic aperture radar signals for enhanced resolution," Ph.D. dissertation, University of Illinois at Urbana-Champaign, Urbana, Illinois, November 1989, Available online: Primary URL <https://engrxiv.org/6a2tn> or secondary URL <https://apps.dtic.mil/sti/pdfs/ADA217178.pdf>.
- [28] J. L. Bauck and W. K. Jenkins, "Tomographic processing of spotlight-mode synthetic aperture radar signals with compensation for wavefront curvature," in *1988 International Conference on Acoustics, Speech, and Signal Processing, ICASSP-88*, vol. 2. New York: Institute of Electrical and Electronics Engineers, April 1988, pp. 1192–1195.
- [29] —, "Convolution-backprojection image reconstruction for bistatic synthetic aperture radar," in *IEEE International Symposium on Circuits and Systems, 1989*. Portland, Oregon: Institute of Electrical and Electronics Engineers, May 1989, pp. 1512–1515 vol.3.
- [30] —, "Convolution-backprojection image reconstruction for bistatic synthetic aperture radar with correction for wavefront curvature and propagation attenuation," in *Millimeter Wave and Synthetic Aperture Radar*, G. K. Huddleston, M. E. Tanenhaus, and B. P. Williams, Eds., vol. 1101, International Society for Optics and Photonics. SPIE, 14 August 1989, pp. 11–18. [Online]. Available: <https://doi.org/10.1117/12.960509>
- [31] M. Rodriguez-Cassola, S. V. Baumgartner, G. Krieger, and A. Moreira, "Bistatic TerraSAR-X/F-SAR spaceborne-airborne SAR experiment: Description, data processing, and results," *IEEE Transactions on Geoscience and Remote Sensing*, vol. 48, no. 2, pp. 781–794, Feb 2010.
- [32] I. Walterscheid, T. Espeter, A. R. Brenner, J. Klare, J. H. G. Ender, H. Nies, R. Wang, and O. Loffeld, "Bistatic SAR experiments with PAMIR and TerraSAR-X—setup, processing, and image results," *IEEE Transactions on Geoscience and Remote Sensing*, vol. 48, no. 8, pp. 3268–3279, Aug 2010.
- [33] D. Fleisch and L. Kinnaman, *A Student's Guide to Waves*. Cambridge, United Kingdom: Cambridge University Press, 2015.
- [34] P. Moon and D. E. Spencer, *Field Theory for Engineers*. Princeton, New Jersey: D. Van Nostrand Company, Inc., 1961.
- [35] L. Sorsa, M. Takala, C. Eyraud, and S. Pursiainen, "A time-domain multigrad solver with higher-order Born approximation for full-wave radar tomography of a complex-shaped target," *IEEE Transactions on Computational Imaging*, vol. 6, pp. 579–590, 2020.
- [36] D. E. Dudgeon and R. M. Mersereau, *Multidimensional Digital Signal Processing*. Englewood Cliffs, NJ: Prentice-Hall, 1984.
- [37] M. van Ginkel, C. L. L. Hendriks, and L. J. van Vliet, "A short introduction to the Radon and Hough transforms and how they relate to each other," Imaging Science & Technology Department, Delft University of Technology, Lorentzweg, The Netherlands, Tech. Rep. QI-2004-01, 2004.
- [38] J. L. Bauck, "A note on Fourier transform conventions used in wave analyses," *EngrXiv.org*, July 2018. [Online]. Available: <http://engrxiv.org/jyt96/>
- [39] S. D. Fisher, M. A. Richards, and G. A. Showman, "An inverse polar format algorithm for turntable spotlight ISAR imaging systems using stepped frequency waveforms," in *Proceedings of the 2004 IEEE Radar Conference (IEEE Cat. No.04CH37509)*. Philadelphia, Pennsylvania, USA: Institute of Electrical and Electronics Engineers, April 2004, pp. 212–217. [Online]. Available: <https://ieeexplore.ieee.org/document/1316424>
- [40] A. W. Rihaczek, *Principles of High-Resolution Radar*. New York: McGraw-Hill Book Company, 1969.
- [41] M. A. Richards, J. A. Scheer, and W. A. Holm, Eds., *Principles of Modern Radar: Basic Principles*. Edison, New Jersey: Scitech Publishing, an imprint of Institution of Engineering & Technology, 2010, vol. I.
- [42] A. Ribalta, "Time-domain reconstruction algorithms for FMCW-SAR," *IEEE Geoscience and Remote Sensing Letters*, vol. 8, no. 3, pp. 396–400, May 2011.
- [43] B.-C. Wang, *Digital Signal Processing Techniques and Applications in Radar Image Processing*. Hoboken, New Jersey: John Wiley & Sons, Inc., 2008.
- [44] J. L. Bauck, "Brief analysis of aliasing in polar and keystone formats in spotlight synthetic aperture radar," *EngrXiv.org*, October 2019. [Online]. Available: <https://engrxiv.org/7dextn/>
- [45] H. J. Cho, "Autofocus and back-projection in synthetic aperture radar imaging," Ph.D. dissertation, University of Michigan, 2016. [Online]. Available: [https://deepblue.lib.umich.edu/bitstream/handle/2027.42/135868/zzon\\_1.pdf](https://deepblue.lib.umich.edu/bitstream/handle/2027.42/135868/zzon_1.pdf)
- [46] S. Basu and Y. Bresler, "O(n<sup>sup</sup> 2/log/sub 2/n) filtered backprojection reconstruction algorithm for tomography," *IEEE Transactions on Image Processing*, vol. 9, no. 10, pp. 1760–1773, Oct 2000. [Online]. Available: <https://ieeexplore.ieee.org/document/869187>
- [47] M. D. Desai, "A new method of synthetic aperture radar image reconstruction using modified convolution backprojection algorithm," Ph.D. Dissertation, University of Illinois at Urbana-Champaign, Urbana, Illinois, 1985. [Online]. Available: <https://apps.dtic.mil/dtic/tr/fulltext/u2/a170652.pdf>
- [48] C. D. Knittle, N. E. Doren, and C. V. Jakowatz, "A comparison of spotlight synthetic aperture radar image formation techniques," Sandia National Laboratories, Albuquerque, New Mexico 87185 and Livermore, California 94550, Tech. Rep. SAND96-2460, October 1996. [Online]. Available: <https://www.osti.gov/servlets/purl/399697>
- [49] A. W. Doerry, "Basics of polar-format algorithm for processing synthetic aperture radar images," Sandia National Laboratories, Albuquerque, New Mexico 87185 and Livermore, California 94550, Sandia Report SAND2012-3369, May 2012. [Online]. Available: <https://ntrl.ntis.gov/NTRL/>
- [50] M. D. Desai and W. K. Jenkins, "Convolution backprojection image reconstruction for spotlight mode synthetic aperture radar," *IEEE Transactions on Image Processing*, vol. 1, no. 4, pp. 505–517, October 1992. [Online]. Available: <https://ieeexplore.ieee.org/document/199920>
- [51] C. V. Jakowatz, Jr. and N. Doren, "Comparison of polar formatting and back-projection algorithms for spotlight-mode SAR image formation," in *Algorithms for Synthetic Aperture Radar Imagery XIII*, E. G. Zelnio and F. D. Garber, Eds., vol. 6237, International Society for Optics

- and Photonics. SPIE, 2006, pp. 137 – 143. [Online]. Available: <https://doi.org/10.1117/12.673249>
- [52] M. Rodriguez-Cassola, P. Prats-Iraola, G. Krieger, A. Reigber, and A. Moreira, “Bistatic SAR image formation: A systematic approach,” in *2014 IEEE Geoscience and Remote Sensing Symposium*, July 2014, pp. 3945–3948.
- [53] M. Rodriguez-Cassola, P. Prats, G. Krieger, and A. Moreira, “Efficient time-domain image formation with precise topography accommodation for general bistatic SAR configurations,” *IEEE Transactions on Aerospace and Electronic Systems*, vol. 47, no. 4, pp. 2949–2966, OCTOBER 2011.
- [54] C. E. Yarman, B. Yazici, and M. Cheney, “Bistatic synthetic aperture inversion for arbitrary flight trajectories,” in *Algorithms for Synthetic Aperture Radar Imagery XIV*, E. G. Zelnio and F. D. Garber, Eds., vol. 6568, International Society for Optics and Photonics. SPIE, 2007, pp. 59 – 66. [Online]. Available: <https://doi.org/10.1117/12.719710>
- [55] —, “Bistatic synthetic aperture radar imaging for arbitrary flight trajectories,” *IEEE Transactions on Image Processing*, vol. 17, no. 1, pp. 84–93, January 2008. [Online]. Available: <https://ieeexplore.ieee.org/document/4392497>
- [56] A. Reigber, M. Jager, A. Dietzsch, R. Hansch, M. Weber, H. Przybyl, and P. Prats, “A distributed approach to efficient time-domain SAR processing,” in *2007 IEEE International Geoscience and Remote Sensing Symposium*, July 2007, pp. 582–585.
- [57] C. Prati, A. M. Guarnieri, and F. Rocca, “Spot mode SAR focusing with the  $\omega - K$  technique,” in *[Proceedings] IGARSS'91 Remote Sensing: Global Monitoring for Earth Management*, vol. 2. IEEE, June 1991, pp. 631–634.
- [58] A. S. Milman, “SAR imaging by omega-k migration,” *International Journal of Remote Sensing*, vol. 14, no. 10, pp. 1965–1979, 1993. [Online]. Available: <https://doi.org/10.1080/01431169308954015>
- [59] R. C. Heyser, *Time Delay Spectrometry: An Anthology*, J. R. Prohs, Ed. New York: Audio Engineering Society, 1988. [Online]. Available: [http://www.aes.org/technical/documents/openaccess/AES\\_TimeDelaySpectrometry.pdf](http://www.aes.org/technical/documents/openaccess/AES_TimeDelaySpectrometry.pdf)



**Jerald “Jerry” Bauck** (Life Senior Member, IEEE) is a researcher, consultant, and inventor living in Tempe, Arizona, USA. He received a Bachelor’s degree from Kansas State University and Master’s and Ph.D. degrees from the University of Illinois at Urbana-Champaign, all in electrical engineering. Dr. Bauck’s research interests include synthetic aperture radar, novel signal sampling methods, and head-related stereophony.